Title
Design and characterization of a neutraized-transport experiment for heavy-ion fusion

Authors
Henestroza, E.
Eylon, S.
Roy, P.K.
et al.

Publication Date
2004-03-14

Design and Characterization of a Neutralized-Transport Experiment for Heavy-Ion Fusion

E. Henestroza, S. Eylon, P. K. Roy, S. S. Yu,
A. Anders, F. M. Bieniosek, W. G. Greenway, B. G. Logan,
R. A. MacGill, D. B. Shuman, D. L. Vanecek, and W. L. Waldron, *LBNL*
W. M. Sharp and T. L. Houck, *LLNL*
R. C. Davidson, P. C. Efthimion, E. P. Gilson, and A. B. Sefkow *PPPL*
D. R. Welch and D. V. Rose, *MRC*
C. L. Olson, *SNL*

Abstract

In heavy-ion inertial-confinement fusion systems, intense beams of ions must be transported from the exit of the final focus magnet system through the fusion chamber to hit millimeter-sized spots on the target. Effective plasma neutralization of intense ion beams in this final transport is essential for a heavy-ion fusion power plant to be economically competitive. The physics of neutralized drift has been studied extensively with particle-in-cell simulations. To provide quantitative comparisons of theoretical predictions with experiment, the Virtual National Laboratory for Heavy Ion Fusion has completed the construction and has begun experimentation with the Neutralized Transport Experiment (NTX). The experiment consists of three main sections, each with its own physics issues. The injector is designed to generate a very high-brightness, space-charge-dominated potassium beam while still allowing variable perveance by a beam aperturing technique. The magnetic-focusing section, consisting of four pulsed magnetic quadrupoles, permits the study of beam tuning, as well as the effects of phase space dilution due to higher-order nonlinear fields. In the final section, the converging ion beam exiting the magnetic section is transported through a drift region with plasma sources for beam neutralization, and the final spot size is measured under various conditions of neutralization. In this paper, we discuss the design and characterization of the three sections in detail and present initial results from the experiment.

I. Introduction

The final transport section in a heavy-ion inertial-confinement fusion system poses major challenges. After exiting the final-focus magnet system, intense beams of ions with a current totaling tens of kiloamperes must drift without further external focusing to the center of a target chamber, a distance of about 6 m in recent conceptual designs [1]. To obtain adequate target gain, these beams must all hit millimeter-sized spots on the ends of the cylindrical fusion target.

From the very early days of heavy-ion fusion (HIF), final focusing has been a subject of intense study [2, 3, 4], with perhaps the most comprehensive study being that of HIBALL-II [5]. These studies assumed that the chamber could have a sufficiently high vacuum that beam ions would experience no forces other than their collective space charge during the final transport to the target. In this final drift section, the beam space charge acts to enlarge the focal spot, so the beam species, current, and energy in early studies were chosen to make the space-charge blowup manageable. For example, Olson

[3] favored a baseline case using 30 kA of 10-GeV U^{+1} ions in a moderate vacuum of 10^{-4} – 10^{-3} Torr. Numerical and experimental studies indicate that ballistic transport could, in fact, be feasible. A 1998 scaled experiment [6] based on the HIBALL-II final-focus design was performed at Lawrence Berkeley National Laboratory (LBNL), obtaining excellent agreement between theory and experiment. Also, detailed numerical simulations of driver-scale systems show good spot sizes for the Olson parameters [7].

Since the HIBALL-II study, however, several significant shifts in conceptual designs for HIF drivers have made ballistic chamber transport unfeasible. One change has been the development of indirect-drive targets [8], which give a more symmetrical energy deposition on the deuterium-tritium capsule than the direct-drive HIBALL-II target but which require more energy to heat the cylindrical metal "hohlraum" enclosing the capsule. At the same time, driver economics has pushed the HIF program toward beams with lower kinetic energy, at the cost of requiring higher total beam current. This higher current can be partly offset by using more beams, but even with an ion mass of 200 amu, more than 450 beams would be required to reduce space-charge effects sufficiently to allow ballistic transport. A third development has been the adoption of "thick-liquid" walls as the mainline US approach to protecting the fusion chamber. In HYLIFE-II [9] and more recent designs [1], jets of molten salt fill much of the volume between the target and the chamber interior wall and absorb much of the blast wave and the radiation. The vapor from these jets has a pressure about 0.6 mTorr and consists mainly of Be_2F and LiF. Due to collisional stripping with this gas, a singly charged ion beam develops a wide spread of charge states by the time it reaches the target, with the average charge state being about two. The effective perveance of the beam is not increased by a similar factor because the liberated electrons propagate along with the beam, but the beam itself becomes much more sensitive to the net space-charge field. Finally, the distributed-radiator targets [10, 11] developed in recent years exacerbate the problem of beam focusing by requiring that beam energy be deposited in a narrow annulus on the hohlraum ends, rather than over the entire end surfaces. The gain for these targets degrades if focal radii of the beams exceed two millimeters, in effect requiring beams with a low transverse temperature and net charge.

A recent HIF driver study [1] reconciles these stringent final-focus requirements. A pivotal feature of this design is the use of low-density plasma in the beam line between the final-focus magnets and the chamber to neutralize much of the beam space charge. [12, 13, 14] If there are enough electrons in the volume swept out by a beam, they can be trapped by space-charge potential well of the beam and provide neutralization during the final transport to the target, thus allowing substantial beam currents while still maintaining the low net charge needed for good focus. In addition, after the target has been pre-heated by lower-current "foot" pulses, thermal radiation from the target will photoionize the nearby background gas, providing additional neutralization as the beam approaches.

The Neutralized Transport Experiment (NTX) has been designed to study, on a reduced scale, the physics of the final focus and neutralized transport of beams with high space charge. The experiment was designed as part of the research program developed by the Virtual National Laboratory for Heavy-Ion Fusion, a formal collaboration of Lawrence

Berkeley National Laboratory (LBNL), Lawrence Livermore National Laboratory (LLNL), and Princeton Plasma Physics Laboratory (PPPL). Construction of the experiment at LBNL began in FY01, and the first transport experiments were carried out in the fall of 2002. As the photograph in Fig. 1 shows, the experiment is quite small in scale. Both the current and the energy are orders of magnitude smaller than driver parameters, but we have chosen the beam and lattice parameters so that the transverse dynamics and neutralization physics of NTX closely model a full-scale system. The experiment is designed to survey a wide parameter space, and there are two independent plasma sources to simulate the upstream neutralizing plasma and the photoionized plasma around the target.

The paper summarizes the objectives, design, and initial results of the Neutralized Transport Experiment. The physics of neutralized transport for driver-scale beams is reviewed in Section II and used to explain the scale and experimental goals of NTX. In Section III, we describe the NTX beam-line layout and diagnostic suite, including a detailed description of two new diagnostics developed for NTX: an improved optical technique for mapping the 4-D transverse phase-space of the beam, and a non-intercepting diagnostic to measure the beam charge density. These improved measurement techniques are essential for quantitative validation of code predictions. The beam line has three principal components, the injector, the magnetic-focus lattice, and the neutralized-transport section. Each of these components presents design challenges, and we discuss the design and characterization of each in Section IV. Experimental results from NTX are presented in Section V. Measurements of beam transport through the magnetic lattice are presented first and compared with particle-in-cell (PIC) simulations made using WARP [15]. We then present the corresponding data in the neutralized drift section, along with theoretical results from WARP and the electromagnetic PIC code LSP [12, 13]. Section VI summarizes NTX accomplishments to date and discusses the direction of future work.

II. NTX Objectives

Two quantities are important for choosing the scaled parameters of NTX. The generalized perveance *K,* loosely defined as the ratio of the edge potential of a beam to its kinetic energy [16], characterizes the importance of space charge in the transverse dynamics of a beam, while the unnormalized emittance ε is a measure of the transverse phase-space area [17]. During the final transport, the perveance and emittance are constant in the absence of collisions and non-linear space-charge fields and for any particular choice of the initial beam radius and convergence angle, they determine the transverse beam dynamics during final transport.

Perveance is dimensionless and, for a non-relativistic beam, is given in SI units by

$$K = \frac{1}{4\pi\varepsilon_0}\frac{2ZeI_b}{m_i v_i^3}, \qquad (1)$$

where I_b is the beam current, and Z, m_i, and v_i are respectively the charge state, mass, and velocity of the beam ions. Early analytic work by Olson [3] estimated that the upper perveance limit for ballistic transport is $K \approx 1.6\text{x}10^{-5}$. The earlier HIF designs, which had $K \leq 10^{-6}$, satisfy this criterion comfortably, whereas recent designs typically require a few times 10^{-4}, and the NTX injector can generate beams with values up to about 10^{-3}. This higher perveance has important ramifications for the focusing and final transport of a beam. Since the beam radius increases with perveance when transverse dynamics is dominated by space charge, beams in a modern driver will sample more field aberrations in the final-focus magnets than in older designs, assuming a similar magnet design. These aberrations introduce radial and azimuthal variations in the focal distance, which degrades the focal spot. Due to their high perveance, beam for modern drivers require some form of external neutralization after final focus to have an acceptable focal-spot radius.

The use of low-density plasmas to neutralize space-charge-dominated ion beams during the final transport has been studied analytically and numerically in recent years [18-25]. Due to the thick liquid wall in a modern fusion chamber, it is difficult to fill the inside of the chamber with plasma at the repetition rate of several shots per second needed for a driver. However, it is straightforward to inject a low-density plasma, referred to as a "plasma plug," along the beam path between the last final-focus magnet and the chamber entrance. An ion beam passing through this plasma drags along electrons as it exits, and these commoving electrons then provide substantial neutralization for the beam along the remaining path to the target. Two other processes inescapably generate plasma in the chamber. First, collisions between a beam and the background gas ionize the gas molecules in addition to stripping electrons from beam ions. Second, once the target becomes hot, photons are emitted which photoionizes the background vapor in the region around the target. This photoionized plasma provides additional neutralization during the critical final part of the beam trajectory. None of these three plasma sources alone provides sufficient neutralization [18, 19, 23, 24], but detailed numerical simulations indicate that together they can give a usable beam focal-spot radius. One of the significant theoretical successes in recent years is use of the electromagnetic PIC code LSP to demonstrate the technical feasibility of a driver point design that meets all the constraints imposed by target, focusing, neutronics, and chamber-engineering considerations [1].

In addition to adequate neutralization, the required millimeter-radius focal spots can only be achieved if the transverse emittance of each beam remains sufficiently small during the final transport. In this paper, we define emittance in terms of distribution averages of the transverse coordinates x,y, $x' = dx/dz$, and $y' = dy/dz$ by

$$\varepsilon \equiv (\varepsilon_x \varepsilon_y)^{1/2}, \tag{2}$$

where ε_x and ε_y are the unnormalized edge emittances [17] in the two transverse directions,

$$\varepsilon_x = 4\left(\langle x^2\rangle\langle x'^2\rangle - \langle xx'\rangle^2\right)^{1/2} \tag{3a}$$

and

$$\varepsilon_y = 4\left(\langle y^2\rangle\langle y'^2\rangle - \langle yy'\rangle^2\right)^{1/2}. \tag{3b}$$

This quantity can be increased both by nonlinear space-charge fields in the beam and by higher-order multipoles in the final-focus magnets. The emittance of the beam entering final focus is determined by the value at injection plus what is predicted to be small growth during acceleration and compression. The final-focus magnetic lattice, however, is a potentially significant source emittance growth. The primary function of this magnetic system is to prepare a converging beam for the final transport. To develop the needed convergence angle, a strongly space-charged-dominated ion beam must go through large envelope oscillations, during which chaotic dynamics due to geometric aberrations in the magnetic fields can lead to emittance growth. While these higher-order effects are well known in final-focus systems with negligible space-charge effects, aberrations in space-charge-dominated beams remain an area of active research.

The major objectives of NTX are to study the final focusing and neutralized transport of space-charge-dominated heavy-ion beams, and to validate the physics models in the numerical simulations. To expedite the experiment and minimize the cost, we chose to use a beam with lower-mass ions than in a driver and a particle energy that is four-orders of magnitude smaller. Also, the physical size of the beam line is about a sixth of the corresponding driver section. The remaining beam parameters are chosen to guarantee that results from this low-energy experiment are relevant to the design of a HIF driver. By scaling the equations for transverse dynamics in the same manner as an earlier scaled final-focus experiment [6], we find that driver-like dynamics is obtained by using the same perveance, reducing the emittance and initial beam radius by the ratio of lattice lengths, and scaling the final-focus magnetic fields appropriately with the ion mass and speed.

This scaling is easily shown to preserve the beam response both to the final-focus quadrupole fields and to any higher-order magnet aberrations. A low-energy beam will therefore have the same envelope trajectory and emittance-growth characteristics as a high-energy beam with the same perveance, provided that image forces and interaction with any background gas are negligible, making the NTX final-focus lattice a good model of a driver-scale lattice.

A small-scale experiment can also address key aspects of driver-scale neutralization physics. Theoretical work by Olson [4], as well as the results of recent simulations [23], indicates that the degree of neutralization from a plasma plug depends principally on the perveance, provided that the plasma has sufficiently high charge density and is in contact with a metal wall that can emit electrons. Space-charge-limited emission at this boundary is crucial because emitted electrons replace those captured by a passing ion beam and thereby maintain the quasineutrality of the plasma. The physics of beam neutralization by the photoionized plasma around the target is likewise determined mainly by the beam perveance and is modeled on NTX by generating a plasma with an appropriate density near the beam focal point.

The final objective of NTX is to make detailed, quantitative comparisons of experimental data with the results of numerical simulations. These comparisons will both help refine the numerical models in the simulation codes and guide improvements in the experimental design and operation. A clear demonstration of the predictive capability of these codes will justify our reliance on them for designing later experiments.

Of course, several driver issues cannot be addressed on NTX. Due to the low current on the experiment, no self-focusing by the beam net current will occur and indeed is only expected to be minor at driver parameters. Image forces in the magnetic-transport section are likewise negligible on NTX. Cross-sections for collisional ionization of the beam and background gas have very different cross-sections for low and high-energy ions, so the effects of collisions cannot be modeled in a scaled experiment. The effects of many beams overlapping as they converge on a target are obviously missing from a single-beam experiment like NTX, and finally, photoionization of a beam by X rays from the heated target cannot be studied due to the lack of suitable radiation source. Future experiments on a larger scale than NTX are needed to investigate these questions.

III. NTX Layout and Diagnostics

IIIA. Beam Line and Parameters

NTX uses a 300-400 keV beam of singly charged potassium ions to study the final focusing and plasma neutralization of a strongly space-charge-dominated ion beam. The energy, which is small compared with typical driver energies, was determined by the decision to use a pulsed-power source used from an earlier experiment. However, as discussed in Section II, NTX replicates driver-like transverse dynamics by a careful choice of beam and lattice parameters. The beam source is designed to produce a current of 75 mA, corresponding to a perveance of about 10^{-3}, and we use beam aperturing to achieve the goals of variable perveance and low emittance. The apertures inserted after the source allow the current and perveance to be reduced by as much as an order of magnitude, and excluding the less intense portion of the beam near the edge simultaneously reduces the beam emittance and increases the brightness.

The drawing of the NTX beam line in Fig. 2 shows the layout and scale of the experiment. Pulsed power is provide by the same Marx generator that was used in the Multiple Beam Test Experiment (MBE-4) [26]. This generator can deliver a pulse of up to 500 kV with a maximum duration of about 20 μs. A timed crowbar switch on NTX produces pulse with a rise time of 0.5 - 1 μs and a "flat-top" of about 10 μs. The remaining NTX components were designed specifically for the experiment and consist of three major sections: a low-emittance potassium gun [27], a magnetic transport section with four pulsed quadrupoles [28], and a one-meter long drift section with plasma neutralization [29].

The K^+ beam is produced on a standard hot-plate source [30], with the perveance being determined by passing the beam through a metal aperture after the diode. Negatively biased rings on either side are used to capture electrons liberated by ions striking the

aperture plate. Aperturing, of course, changes the beam emittance as well as the perveance, but WARP simulations show that dynamics in the final-focus lattice is insensitive to emittance for the space-charge-dominated NTX beam.

Although the NTX beam typically has a 2-cm radius as it enters and exits the magnetic-transport section, the magnets nonetheless have a 15-cm radius bore. Any four-magnet focusing system gives the beam a large radial excursion before the last magnet, and in NTX, we want to handle perveances that are substantially higher than expected in a driver, so the large bore is used to accommodate large radius swings while still keeping the beam away from the more nonlinear magnetic fields near the wall. The choice of a 60-cm half-lattice period and 2.4-m total length followed from practical considerations, such as the available power supplies for the magnets and limits on the overall length of NTX.

The layout of the 1-m NTX plasma neutralization section is shown in Fig. 3, and the sketch in Fig. 4 shows how it functions. The upstream plasma, modeling the "plasma plug" that neutralizes the beam after it exits the final-focus section, consists mainly of electrons and doubly charged aluminum ions from a pulsed cathode-arc source (sometimes called a metal-vapor vacuum arc or MEVVA source). The plasma itself is centered 0.25 m after the end of the last magnet so that it is well away from the fringe fields, and it extends about 0.05 m in both directions. After the beam exits this first plasma, it drifts 0.75 m through a 3.5-cm radius beam pipe into a six-way cross at the nominal focal point. A second plasma generated at the center of the cross simulates the photoionized gas that will surround a target hohlraum after it has been heated by early low-current "foot" pulses. This "target" plasma is generated by a pulsed radio-frequency (rf) source and has a charge density approximating that expected in a fusion chamber. A diagnostic box is placed after the focal point.

IIIB. Diagnostics

The initial measurements of the NTX beam were made with the same diagnostic tools used on MBE-4 [26, 31] and other early HIF experiments. A diagnostic box containing various combinations of slits and Faraday cups was moved to the end of each NTX section as the experiment was being assembled, and the beam was characterized at each of these points. A Faraday cup, with a 2-cm entrance radius and a guard ring biased to exclude electrons, was used to make time-dependent current measurements, and a "slit-cup," consisting of a moveable slit with an attached Faraday cup to measure the transmitted current, measured the line-integrated beam profile. A second moveable slit was used along with the slit-cup to map out the transverse phase space of the beam by a standard double-slit technique [32]. The slit and the slit-cup, aligned in parallel to the first slit and located behind it, are moved so as to sample either the (x, x') or (y, y') phase space, as sketched in Fig. 5, with the collected current being recorded for typically 400 or more shots. These data are then used to construct contour plots of phase-space density in the various two-dimensional (2-D) planes. The response time of the Faraday cup allows a time resolution of about 150 ns. In addition to transverse emittance, these data yield other time-resolved quantities, such as the beam size, centroid position, and density profile.

In addition to these conventional diagnostics, NTX now uses optical diagnostics to furnish detailed, time-resolved information about the ion-beam transverse phase space. Work has also begun to characterize a non-intercepting electron-probe technique that will furnish information about the transverse structure of the beam charge density. The design and implementation of these diagnostics are discussed in the following subsections.

Optical diagnostics

We have developed an optical diagnostic technique for NTX as a faster and more flexible alternative to the double-slit technique. This optical technique, which is related to the gated beam imager (GBI) [33], uses scintillator plates imaged by an image-intensified charge-coupled-device (CCD) camera. The GBI uses a "pepper-pot" to create an array of beamlets that are imaged directly onto a gated microchannel plate (MCP). The new NTX technique differs in two ways. First, a thin sheet of scintillator material is substituted for the MCP imager, allowing the MCP to be placed away from the beam line with the camera. Second, a single movable pinhole replaces the pepper-pot because the convergence of the NTX beam would cause side-by-side beamlets to merge. The technique is simple, compact, and more flexible, because only the scintillator material is placed in the path of the beam. More NTX shots are needed to map out the beam phase space, but this requirement is manageable due to the reproducibility of the NTX beam and the ease of each measurement.

We have used glass and ceramic (98% alumina) as scintillator materials. Charge neutralization is provided by a high-transparency (80-90% transmission) metallic mesh placed on or near the surface of the scintillator. Beam ions striking the mesh generate secondary electrons. Since the secondary electron yield is on the order of 10 or greater for the beams of interest, sufficient electrons are created on the mesh to charge-neutralize the insulating surface. In addition, by applying a negative bias to the mesh, stray external electrons are decelerated and deflected away from the scintillator, limiting their contribution to the optical image to negligible levels.

The measured rise time of the scintillator is less than 50 ns. There is no evidence for saturation or thermal quenching in the scintillator response. We tested linearity over the range of measured intensities by imaging the same beam in horizontal and vertical slit scans. The local intensities in the two scans differed by an order of magnitude, but the summed intensities of all images in each of the two scans agreed. The lifetime of the scintillator material under intense ion beam bombardment is limited, but the current and energy of NTX are sufficiently low that this limitation is not a concern.

Time-resolved beam-induced images on the scintillator screen are captured with a Roper Scientific gated intensified CCD camera viewing the scintillator through a vacuum window, and images are processed using the public-domain program ImageJ. Figure 6 shows a typical beam image taken on NTX near the focal point. The neutralized beam is seen to form a sharp spot, and the quadrupole distortion from final-focus aberrations is clearly visible.

Whole-beam scintillator images like Fig. 6 are the primary optical diagnostics reported in this paper, but a scintillator-based imaging technique is also being used now to map the four-dimensional (4-D) phase-space distribution of the NTX [29]. The phase-space distribution $f(x,y,x',y')$ is measured over many shots by scanning the beam cross section with a movable pinhole having a diameter of 5×10^{-4} m (20 mils). The transmitted beamlet then travels to the nominal focal point, about ~1 m where it strikes the scintillator plate. The position of the pinhole defines the coordinates x and y, and from the image, we can extract the density distribution of x′ and y′. Figure 7 shows this technique schematically, along with selected images of the individual beamlets that reveal a very detailed phase-space structure. A detailed knowledge of the 4-D phase space is essential both for more-realistic initialization of neutralized-transport simulations and for understanding the NTX experimental results.

Non-interception charge-density diagnostic

All the NTX diagnostics mentioned above entail inserting apparatus temporarily into the beam line, either blocking or significantly altering the ion beam. Moreover, since characterization is not done simultaneously with experiments, there is a possibility that beam parameters may drift.

As an alternative, we are developing a non-intercepting beam diagnostic to characterize an ion beam during its operation. By repeatedly measuring the deflection of a low-current electron beam propagating across the NTX beam, we can map out the transverse charge density of the ion beam. The sub-millimeter electron beam has a current of 1-5 μA current and an energy of 5-8 kV. A chicane of four magnets, labeled D1-D4 in Fig. 8, first deflects its trajectory some chosen distance above or below the beam axis, and then on the other side of the NTX beam line, deflects it back approximately to the original plane, where its position is registered on a scintillator for optical analysis. The current and energy of the electron beam are chosen so that it will not perturb the NTX beam but will itself be significantly deflected. Provided that the electron-beam space charge is negligible, the beam will be deflected at a predictable angle that depends on the charge-density distribution of the NTX beam, integrated along the electron-beam trajectory. By varying the strength of the magnetic fields on a series of NTX shots, the electron beam can pass through every part of the ion beam, and the scintillator detects the resulting deflections as functions of time along each pulse.

Figure 9 shows a photograph of the assembled diagnostic box, with the electron gun, magnets, and scintillator all placed inside a vacuum chamber maintained at better than 1×10^{-7} Torr. The commercial electron gun has a LaB_6 cathode that operates at energy of 5 -10 keV and delivers a beam current that meets the requirement of 1 - 2 μA. The dipoles D1 –D4 are iron-dominated to minimize current requirement and provide high field uniformity, and they are designed to operate inside the vacuum chamber with the cathode. The detector is a Yttrium Aluminum Perovskite (YAP:Ce) scintillator with a 100-nm aluminum coating on the front surface to drain accumulated charge. A CCD camera is focused on the scintillator and is connected to a computer to record image data. We measure ± 3-cm vertical displacement of the electron beam while varying current

through magnets D1 and D2, affirming that this diagnostic can scan an ion beam with a diameter up to 6 cm.

Since this diagnostic is not used for the results presented in this paper, design details are presented elsewhere, along with preliminary experimental findings [34]

IV. Key NTX Components

The three principal sections of NTX have unusual requirements and are therefore described in detail in the following subsections. In order to explore aberrations in magnetic transport and effects of incomplete neutralization, an ion source with a variable perveance and a very low emittance has been designed and tested. The source characteristics are summarized in Section IVA. The pulsed quadrupoles for final focusing must have excellent field quality so as not to introduce unwanted aberrations due to magnet imperfections. The design, construction, and measurements of these magnets are presented in Section IVB. Finally, in Section IVC, we summarize the design and characterizations of the plasma sources used in the neutralized-drift experiment.

IVA. Variable-Perveance Ion Source

The NTX experiments require a beam current that can be varied by one order of magnitude, up to 75 mA. This variability is needed both to investigate the effects of aberrations in final focus and to test the sensitivity of plasma neutralization to beam current. In addition, neutralization studies also require a high source brightness, a quantity roughly proportional to the beam current divided by the square of its emittance [35]. The use of aperturing to vary the perveance simultaneously generates high-brightness beams by removing the edge of the beam after it exits the diode. Beam scraping, however, produces secondary electrons that must be controlled. Stray electrons can introduce nonlinear space-charge forces, which can lead to an increase of the transverse emittance [36] and, in extreme cases, to beam disruption. In NTX, we control the secondary electrons by placing electron traps near the beam scraper. Each of these electron traps has a sufficiently large negative potential to confine the electrons even in the presence of the positive ion-beam self-field.

A photograph of the ion gun, together with the beam aperture and electron-trapping device is shown in Figure 10. The 75-mA K^+ beam is produced on the surface of a 2.54-cm diameter alumino-silicate source [30] heated to 1060^{o}C, and it exits the 12-cm diode gap with an energy of 300 - 400 keV. The beam aperture, with holes of variable diameter, is placed about 8 cm beyond the diode exit plate, sandwiched between two metal rings of 5-cm length and 6.2-cm inside diameter. The nominal -3 kV bias on these rings provides adequate trapping of the free electrons produced by ions striking the aperture. The EGUN [37] calculation in Fig. 11 shows potential contours and steady-state ion trajectories for this nominal case.

We first characterized the diode without an aperture plate. The peak current at 400 kV is 77 mA, which agrees within the uncertainty of the measurement with the EGUN

prediction of 73 mA. The measured current follows the familiar Child-Langmuir scaling [38] as the voltage is varied by a factor of three. The measured beam profile and emittance show small deviations from uniformity due to known imperfections in the beam optics. We then inserted an aperture of 2-cm diameter and applied the nominal electron-trap voltage. The measured current is 55% of the total, again consistent with the EGUN prediction. The density profile of the apertured beam is found to be much more uniform, and the emittance in each of the transverse directions is lower by a factor of two, producing overall a doubling of brightness.

When the ion beam is apertured and a negative bias voltage of 3 - 6 kV is used to capture electrons, the measured beam profile is quite uniform. The slit-integrated density profile shown in Fig. 12 for a 25-mA beam deviates from the corresponding EGUN calculation by a maximum of 2%, with the average deviation being much smaller. The measured emittance is less than a factor of two above the value expected from the source temperature alone ($\square$~ 7.5 π mm-mr). The only significant qualitative difference between the experimental phase-space plots in Fig. 12 and the corresponding computer-generated plots is a slight S-curve deviation in x' resulting from a third-order ("spherical") aberration in the NTX focusing system. The K^+ beam in Fig. 12, with energy of 300 keV and $\square$~ 12.5 π mm-mr, is used for the neutralized-transport experiments reported here.

IVB. Final-Focus Lattice

The NTX magnetic-transport section is designed to correspond closely to a typical HIF driver final-focus lattice. The section consists of four pulsed quadrupole magnets separated by short drift regions, plus the drift regions at the two ends. The three-dimensional (3-D) layout of the magnets and the beam source is shown in Fig. 13.

Figure 14 shows the horizontal and vertical beam envelopes through the system, both with and without ideal beam neutralization after the final-focus lattice. The quadrupole fields are chosen to obtain a beam with 1-m focal length (20-mm radius and 20-mr convergence angle) at the entrance to the neutralization region. The beam is quite large in the two center magnets, which determines the required bore size and winding radius. Each magnet has a relatively short center section, and a substantial portion of the magnetic field is contained in the end fringe fields, which have significant axial components. Due to the large radius fluctuations in the focusing magnets, ion-beam dynamics is highly non-paraxial. Consequently, the usual beam-axis-integrated method of representing fields by normal multipoles of discrete length does not give accurate particle trajectories in simulations, because these hard-edge field approximations omit the axial field components and nonlinear radial gradients that are major sources of particle deflection. Particle-tracking simulations therefore require the knowledge of the full multipole content of the magnetic field. Previous work [39] has shown that, to second order, the main magnetic-field multipoles contributing to beam dynamics are the normal quadrupole, the normal sextupole, and the pseudo-octupole components. These three components are included in all the numerical simulations used in designing of the NTX lattice, so 3-D magnetic analysis is essential.

Magnetic field modeling

Each magnet is a current-dominated quadrupole, with eight conductor turns per coil in a single layer, arranged inside a cylindrical laminated-iron return core. A 3-D finite-element model of the magnets was generated using the ANSYS/Emag program and was solved for the static field in 3-D space. A scalar potential formulation is used, with source current elements used for the coil. The space modeled is a $1/8^{th}$ section of one half the magnet, shown in Fig. 15. Far-field (infinite boundary) elements bound the outer radius and end, at a distance 75 cm from the magnet midplane, which extends well past the source and final focus points. A cylindrical Neumann boundary is used to simulate the steel core, in order to speed analysis when a fine mesh is used. This choice is acceptable because an earlier coarse-mesh model with steel included showed no significant saturation.

The resulting 3-D field maps generated were decomposed into both normal and pseudo multipoles as a function of distance in the axial direction. Figure 16 shows these multipoles as a function of longitudinal distance z. Both half-octant models and full-magnet finite-element models, complete with spiral coil geometry, crossovers, and leads, were computed to determine both symmetry-allowed and full-skew (normal and skew) multipoles, respectively. The higher-order normal multipoles are comparatively unimportant. Finally, we performed beam-tracking simulations through the lattice of focusing elements generated by superposition of these field maps.

Magnet design and fabrication

The NTX magnet design differs from the initial specification [40] in the choice of a larger bore and winding radius, as well as in the simpler coil design. Table 1 gives the final design and operating parameters.

The magnets were fabricated using a simplified, single-layer coil design, featuring a novel diagonal leadout. The diagonal leadout from the inner turn approximates the staircase-pattern of "missing" currents that are inherently present in any spiral coil. This leadout design allows short coils with few turns to have relatively high field symmetry. This concept is sketched in Fig. 17.

Each magnet is driven by a capacitor, which is discharged through a series string of thyristors to produce a half-sine wave current pulse. We use a 2-mF capacitor to achieve

Beam Aperture Radius, R_b	14.9	cm
Magnet Winding Radius, R_w	17.32	cm
Steel Inner Radius, R_w	18.33	cm
Steel Outer Radius, R_o	25.63	cm
Mag., Total Lengths, L_m, L_o	46, 50	cm
Magnet to magnet spacing	60	cm (ctr.-ctr.)
Field Gradient, B'	2-5	T/m
Maximum Field, B	0.6	T, @12cm
Number of turns, N	8	Turns/coil
2-D Field Coefficients, B_n ($\square n\|A_n\|/2A_2$, n=6,10,…,26)	$7x10^{-4}$	T/T @10cm
Conductor diameter, d_c	4.65	mm
Magnet Current, $I_{min.}$ - I_{max}	3.3- 8.2	kA
Magnet Resistance, R	.036	$\square$
Magnet Inductance, L	232	$\square$H
Pulse length (full half sine), t	2.2	ms
Magnet Voltage, max., V	2.7	kV
Pulse energy, max., U	7.8	kJ
Energy loss/pulse, max., Q_t	2.7	kJ
Max., Operating Pulse Rates	0.5, 0.1	Hz
Temp. Rise, Max., steady state	25	°C, (0.5Hz P.R)

Table 1. Magnet Parameters

the full current with minimal voltage and to increase the pulse length, thus reducing eddy currents. Bipolar charging of the capacitor is used to decrease the voltage that appears between the magnet and the grounded housing by a factor of two compared to unipolar charging.

We performed 2-D transient magnetic modeling to determine the effect of eddy currents in surrounding components, such as beam tubes, flanges, diagnostics, and electron traps. Eddy currents in the beam pipe are found to be acceptable, with a 7.4% loss of peak field and a 0.28 ms field peak time lag from the source current peak, as shown in Fig. 18.

Six quadrupoles have been fabricated in order to provide two spares, one of which has been subjected to 10^4 full-current pulses for testing reliability. The other magnets have been subjected to 10^3 full-current pulses for acceptance testing. No cooling, other than free air convection is necessary. Figure 19 shows one of the coils during fabrication.

Magnetic field characterization

The selection of measuring technique for the quadrupole magnetic field was determined by two factors. First, the beam envelope varies significantly within the magnet ruling out techniques such as rotating (harmonic) coils that generate an axially integrated field measurement. It was necessary to obtain a three-dimensional field map. Second, the magnets are pulsed. Cooling requirements prevented the magnets from being operated continuously except at relatively low fields that compromised the accuracy of the

measurement. We also wanted to study the effect of eddy currents in the beam pipe on the magnetic field. Measurements of a pulsed field limited the use of Hall probes and other commercially available probes.

We characterized the quadrupoles using simple pickup loops to monitor the changing flux as the magnets are pulsed. The probe design, sketched in Fig. 20, balances the competing considerations of accuracy, signal strength, and ease of fabrication. Three separate pickup loops are incorporated into each probe to permit the measurement of the magnetic field vector. Each loop has 20 turns (2 layers of ten turns) of 0.13-mm (5-mil) copper wire. The three cross sections are slightly different diameter to minimize mechanical interference between sets of windings. Four of these probes are spaced equally around a disk at a 10-cm radius and mounted on a supporting cylinder inserted into the magnet bore. The cylinder can be rotated about its axis or adjusted vertically and horizontally, and the magnets are moved longitudinally on rails so the probes can sample different axial positions.

We have two different modes of field measurements. For initial characterization, the axis of the supporting cylinder is aligned with the magnet mechanical axis. With the probes positioned lengthwise near the center of the magnet, the cylinder is rotated to maximize either the radial or azimuthal field for the four probes. Measurements are then recorded as the cylinder is rotated in 15-degree increments for 90 degrees. The magnet is shifted axially, and measurements are taken again as the cylinder is rotated back in 15-degree steps to the starting angle. This process is repeated with the probes near each end of the magnet. Each measurement records all three components of the field vector at four positions. Although this is a very sparse field mapping, any fabrication problems will stand out. The second mode entails a detailed mapping the field over a constant radial position relative to the magnet axis. These data are then used both to determine the tilt and offset of the quadrupole field axis with respect to the mechanical axis and to identify higher order modes.

Output from the probes is shown in Figure 21. The signal-to-noise ratio is excellent for probe orientations aligned with the field. Careful adjustment of the rotational position of the probes can reduce at least one of signals to the noise level in the other probe orientation. The field components calculated from the signals are shown in Fig. 22. The applied magnet current is shown with the field plots to demonstrate the fidelity of the system and analysis. Figure 23 compares the measured longitudinal profile of the quadrupole field with the computed profile, where we have normalized the peak fields for comparison.

IVC. Plasma sources

A crucial aspect of NTX is the validation of neutralized transport in the fusion chamber. As described in the introduction, the presently favored concept for neutralization of driver beams involves passing them through a low-density plasma before they enter the fusion chamber. Provided that the plasma is in contact with an emitting surface, the neutralizing electrons remain trapped in the beam potential as the beam exits the plasma, providing charge and current neutralization in the chamber. In addition, the main driver

beams arrive after the hohlraum exterior has been heated to about 100 eV. As these pulses approach the target, they are photostripped by soft X rays from the target and receive further neutralization from the plasma formed around the target by photoionization of the background gas.

NTX uses two plasma sources to mimic the effects of this plasma neutralization. A pulsed cathode-arc source provides an upstream aluminum plasma for the initial neutralization, and a pulsed radio-frequency (rf) source provides a volume plasma near the beam waist. These sources can model the effects of plasma neutralization adequately well, even though they obviously cannot duplicate the collisional scattering or the photostripping that would be found in a driver.

We have used the electromagnetic PIC code LSP [12, 13] to determine the requirements for both plasma sources. Numerical simulations indicate that we require a neutralizing plasma with a length in the range of 10- 20 cm and an electron density that is 1-100 times the nominal initial NTX beam density of about 3×10^8 cm^{-3}. The density of the target plasma, of course, will increase in density as the beam impinges on the target due to continuing photoionization by X rays from the hohlraum. However, the nominal plasma density around the target is expected to be comparable to the final beam density. For NTX, this value will be around 10^{10} cm^{-3}, depending on the perveance and the focal-spot radius.

Cathode-Arc Plasma Source

The pair of pulsed cathode-arc plasma sources shown in Fig. 24 has been designed and fabricated at LBNL for the NTX neutralized-transport experiments. The density and duration of the metal plasma can be adjusted in a very wide range. For example, aluminum plasma of density 10^8-10^{12} cm^{-3} can be produced in pulses of 1-1000 μs by selection of suitable arc current and discharge geometry. These sources have an insignificant fraction of neutral atoms and molecules in the plasma, making them ideal sources for a neutralizing plasma.

The plasma sources are of the "mini-gun" type, consisting of a replaceable cathode rod of 0.625-cm diameter and about 2.5-cm length, a ceramic insulator as part of the cathode assembly, and a grounded anode body [41]. The source is coupled to an open macroparticle and neutral-atom filter [42], consisting of a copper coil with a 90^o bend. The filter removes particles from the plasma stream, allowing only clean, fully ionized metal plasma to reach the NTX beam line. Two of these source/filter assemblies are installed on NTX, injecting plasma from opposing sides to produce a symmetrical plasma distribution. The consumable cathode of each source is made from aluminum, because deposition of aluminum on the beam line's components does not introduce foreign material. The lifetime of the cathode before maintenance is estimated to be about 10^5 pulses.

In initial tests, the two source units (plasma gun and filter) were mounted in a high-vacuum. A large ion collector, made from a flat, isolated sheet of stainless steel, was positioned between the sources. The collector is biased negatively to repel electrons and

collect ions. The plasma ion current is noisy, as is typical for cathodic vacuum arcs. We use the plasma at about 250 μs after arc triggering, just before the second maximum of the plasma current, so we made repeated measurements of the plasma ion current at that time to get information on statistical fluctuations. The result is shown in Figure 25. We then mounted the source units on a large flange to be inserted in the beam line. The flange, with sources and the beam shield, was evacuated with a small turbomolecular pump to a base pressure of about 10^{-5} Torr. To demonstrate the shot-to-shot reproducibility, we show ten successive ion current pulses in Figure 26.

The plasma density can be estimated by noting that the ion current is given generally by $j_i = Zen_i v_i$, where j_i is the ion current density, Z is the average charge state number, e is the elementary charge, n_i is the ion number density, and v_i is the average ion velocity in the direction of the collector, which is here identical with the plasma flow velocity. From previous work [43], we know that $Z = 1.7$, $v_i = 1.54 \times 10^5$ m/s, and with an area of collection of about 10^{-2} m^2, one obtains $n_i \approx 1.8 \times 10^{10}$ cm^{-3} for the average plasma density inside the metal shield at about 250 μs after arc triggering, at a pulse-forming network (PFN) charging voltage of 2.0 kV. This density can be adjusted through a change of the distance between the filter exit and the beam shield, and by the arc current via the PFN charging voltage.

A commercial Langmuir probe from Scientific Systems, together with its accompanying SmartSoft software, was used to measure the density of the aluminum plasma produced by the cathode-arc source as a function of space and as a function of discharge voltage. Since the plasma streams into the beam line at supersonic ion velocities, the analysis algorithms contained in the SmartSoft software cannot be used. However, using the ion saturation current from the measured current-voltage (IV) characteristics and making simplifying assumptions about the aluminum plasma allows us to calculate an estimate of the plasma density. We find that the NTX cathode-arc source produces plasmas with densities in the 10^{10} - 10^{11} cm^{-3} range and that the plasma density is proportional to the discharge voltage over the range from 1.5 kV to 2.5 kV. The measurements show that the plasma density along the axis is peaked at the location of the pair of entry ports where the plasma enters the beam line and drops off over a distance of a few centimeters. At the axial location of the entry ports, the density is greatest near the mouths of the two ports, and decreases towards the axis since the plasma expands as it moves away from the ports.

The Langmuir probe requires 5 μs to acquire each data point on the IV characteristic, and each IV characteristic is comprised of 200 points. Thus, to obtain the temporal resolution necessary to measure the plasma density at a given instant during the 300 μs cathode-arc discharge, the Langmuir probe is operated in boxcar mode. In boxcar mode, a trigger pulse generated at the desired time during the discharge triggers the Langmuir probe to take a single IV measurement. The cathode-arc system must then be triggered 200 times to acquire a complete IV characteristic. The 10% - 20% shot-to-shot variation of the cathode-arc source is reflected in the scatter of the points in the IV characteristic shown in Fig. 27. Despite these fluctuations, the ion saturation current I_{sat} can be measured from these data and used to calculate the plasma density.

Figure 28 shows the dependence of the ion saturation current on the discharge voltage. Below 1.5 kV, arc triggering does not occur. Operation above 2.5 kV is not possible with the PFN presently in place. The data show that the plasma density can be varied by a factor of four by adjusting the PFN charging voltage.

The axial density profile is shown in Fig. 29 and shows that the axial extent of the plasma is approximately 5 cm and is strongly peaked near the port openings which are located at z = 144 mm here. It should be noted that even though the densities plotted in Fig. 29 are those computed by the questionable SmartSoft algorithm, they are very close to values calculated using the simple model outlined above. Moving the Langmuir probe in the transverse direction allows us to measure the transverse profile of the plasma stream. From the ion saturation current measured at numerous points across the beam path, we find that the plasma expands and the density decreases as the plasma moves away from the ports, and the density is smaller yet near the top of the beam-line tube.

Radio-Frequency Plasma Source

A radio-frequency (rf) plasma source, shown in Fig. 30, has been built at PPPL to model a target plasma on NTX. The goal is to generate plasmas with electron densities up to 10^{11} cm^{-3} and a pressure in the range of 10^{-6} - 10^{-5} Torr, requiring effectively full ionization. The low pressure is important to prevent neutrals from stripping beam ions to higher charge states. Recently, pulsed operation of the rf source has achieved this goal.

The pulsed plasma source has a six-way cross at the center of its design. A turbo-pump attached to one face maintains the vacuum while the gas inlet and the rf quartz window are attached to the opposite face. A three-turn copper spiral antenna is situated inside a shielded box and faces the window. The rf matching network is directly connected to the antenna enclosure and is tuned to match the low impedance antenna to the 50 Ω transmission cable. The drift tube for the ion beam is connected to two flanges on the six-way cross perpendicular to the turbo-pump and antenna. The plasma drifts into the center of the cross, and intersects the propagating ion beam. The source operates by applying a puff of argon gas and a pulse of rf power to the antenna. The potential advantages of pulsed operation are that it can easily operate at high peak rf power levels, and the amount of gas can be limited. The plasma density and the neutral gas pressure are issues primarily during the 100 μs the ion beam passes through the plasma. Consequently, plasma parameters and neutral-gas pressure are dynamic quantities and need to be measured as a function of time in order to evaluate source operation.

A typical ion-gauge controller does not have the time response to measure the quick pressure bursts when a gas puff is applied to the system. However, by measuring the voltage across a resistor placed in series with the collector current of the gauge, the dynamic absolute pressure in the plasma source can be ascertained. The dynamic pressure measurement is calibrated at a fixed pressure while the pressure gauge is read, and the voltage across the resistor is recorded. To insure that the observed rise time is indicative of the rising gas pressure and not the RC time response of the circuit, the pressure measurement for a given plasma condition was repeated with two different resistors with an order-of-magnitude difference in resistance. The pressure evolutions for

the two resistors were in agreement. Applying a 5-ms gas puff to the plasma source, the pressure sharply rises to 2 mTorr and pumps away in about one second. This time scale is expected to be compatible with NTX because the experiment produces 100-μs ion beams every 15 seconds. The plasma electron density was measured with the Langmuir probe. It compensates for measurements in rf fields and can make high time-resolved measurements with reproducible plasmas. The pulsed plasma source was observed to be very reproducible in parameters and breakdown time.

To operate the plasma source, the gas valve and the rf power are triggered at the same time ($t = 0$). In this mode, it is easy to deliver more than 2 kW of rf power to the source, compared to only 1 kW for continuous plasma source operation. The power is measured with a directional coupler and calibrated diode. The source characteristics for a net forward power of ~3.5 kW versus time are shown in Fig. 31. Before $t = 3.75$ ms, the plasma density is less than the sensitivity of the Langmuir probe (~ 10^7 cm^{-3}), and the neutral pressure is below the sensitivity of the dynamic pressure measurement (10^{-6} Torr). The onset of breakdown is clearly observed in the forward and reflected rf power versus time. The rf matching network is adjusted so that there is a maximum net power delivered to the plasma. At $t = 3.75$ ms, the electron density is 10^{11} cm^{-3} and the neutral pressure is simultaneously low. The effective ionization fraction for $t = 3.75 – 4$ ms is in the range of 50 - 100%. At later times, the power density is not sufficient to sustain the ionization fraction, and the neutral density rises faster than the electron density.

One difference between the initial source tests at PPPL and those at LBNL was that the rf generator was unable to provide 3.5 kW of power at LBNL and was limited to 2.5 kW. This lower power limited the maximum plasma density that could be achieved. A number of density measurements were made in the 6-way cross with the Langmuir probe. A profile measurement was made transverse to the axis of the plasma source and turbo-pump (Fig. 32). The density is peaked on axis. There is a factor of two drop near the plasma source wall radius of 5 cm. Distances greater than 5 cm from the center of the cross are hidden from the straight-line path of the plasma out of the source. There, the density decreases by an order-of-magnitude at a distance 5 cm from the wall radius of the plasma source.

Another profile measurement was made in the 6-way cross, but along the axis of the plasma source (Fig. 33). In this direction the plasma has a steep gradient away from the antenna because of the short plasma skin depth (~ 1 cm). This has also been seen in our previous steady-state electron-cyclotron resonance (ECR) plasma sources. Consequently, the plasma density drops by two orders-of-magnitude across the cross diameter in this direction. In the ECR source, a weak magnetic field was used to reduce this, but is not used in the pulsed source. Lastly, a density measurement at the center of the cross as a function of rf power was completed (Fig. 34). The electron density increases exponentially as a function of power. The data point near 3.5 kW was obtained at PPPL, but not at LBNL. Consequently, the source is limited to 5×10^{10} cm^{-3} density for the NTX experiments until the rf generator can produce the higher power levels.

The rf generator will be brought back to its 4-kW power capability in order to achieve the densities observed at PPPL. Furthermore, the gas valve will be replaced with a faster one

to limit the gas introduced to the NTX vacuum system. Lastly, modified versions of the pulsed plasma source may be examined to achieve larger plasmas along the ion beam path.

V. NTX Experimental Findings

The two main areas of NTX research since the experiment was commissioned have been beam transport through the final-focus lattice and the final meter of ballistic transport with and without the neutralizing plasmas. A major part of this research is the comparison of experimental data with the results of numerical simulations.

VA. Magnetic-Transport Experiments

The main issue of the magnetic-transport experiments is the control of emittance growth due to higher-order fields from magnetic multipoles and image fields. Here, we present experimental results from NTX on beam envelope and phase space distributions, and compare these data with the results of particle simulations by the PIC code WARP.

The ion beam extracted from the Pierce-type NTX diode suffers from spherical aberrations, as evidenced from phase-space distortions (high emittance), and from non-uniform density profiles. Since the source of these aberrations is the presence of high-order field components, the particles at the edge of the beam are the most affected. A high-brightness beam is produced on NTX by removing the beam edge after the pulse is generated in the diode [27]. To study beam transport through the final focus system we have used a 300 keV, 25 mA, beam with a emittance of 12.5 □ mm-mr and a uniform density profile. Figure 35 shows the good agreement between the measured (top) and calculated (bottom) beam profile and phase space distribution for the nominal energy (300 keV, 25 mA) and quadrupole field configuration. The figure also shows that the final parameters for the nominal case correspond to that of a beam of the required 1-m focal length (20 mm radius and 20 mr convergence).

The slight distortion of the beam profile was traced back to a small rotation (5 mr) of one of the quadrupoles. The beam is uniform with a narrow rim due to field aberrations and the final beam emittance of the beam is about 25 □ mm-mr, which should allows the beam to be focused to a 1-2 mm focal-spot radius in neutralized-transport experiments. Furthermore, Faraday cup measurements of the beam current at entrance and exit of the final focus system show insignificant beam loss along the transport channel.

We have also performed a complete characterization of the quadrupole lattice by comparing experimental results with particle simulations using the PIC code WARP. Figure 36 shows the good agreement between the calculated (top) and measured (bottom) beam profiles at the exit of the final focus system when the beam energy is varied in steps of 3% around the nominal energy (image at center). The numerical simulations track the beam behavior as the beam expands by a large factor when the energy changes from -9% to +9% around the nominal energy.

We have also compared the measured beam profiles for several quadrupole strengths with the corresponding profiles calculated by WARP. The comparison is shown in Fig. 37. For each quadrupole, the corresponding row shows the profiles for a change of -5%, 0% and +5% from the nominal quadrupole strength. This comparison shows the good agreement that we have obtained so far, between measurements and simulations.

VB. Neutralized drift experiment

An important area of NTX research is studying the effects of beam neutralization on transport. A converging ion beam exiting the final focus magnetic system is injected into a neutralized drift section. As detailed in Section IIIA, neutralization is provided by a metal arc source and an rf plasma source. Both sources deliver reproducible plasmas with densities up to ten times greater than the beam density, a sufficient value for a range of plasma-plug and volumetric neutralization experiments. Effects of a plasma plug, where electrons are extracted from a localized plasma in the upstream end of the drift section, and are then dragged along by the ion potential, as well as the "volumetric plasma", where neutralization is provided by the plasma laid down along the ion path, are both studied and their relative effects on the beam spot size are compared.

Plasma neutralization in NTX is simulated with LSP [12, 13]. Using particles extracted from a WARP simulation as input, we simulate the neutralization process of the focusing beam passing through a plasma and follow the beam past its focal point. The simulation box is 3.8 cm in radius and 130-cm long. The K^+ beam is injected through an open (Neumann) boundary at z = -30 cm and initially has a 2-cm outer radius, a 25-mA current, and a 300-keV energy. At initialization, the plasma extends out to the outer wall and from z = -10–0 cm, with a uniform density of electrons and Al^{+2} ions and a 3-eV temperature. It should be noted that this temperature is comparable to the critical energy $\frac{1}{2}m_e v_i^2 = 4$ eV and could influence the neutralization process to some extent. Where the plasma is in contact with the outer wall, space-charge-limited emission (SCLE) of cold electrons is permitted. This boundary enables the re-supply of low-energy electrons to maintain quasi-neutrality of the plasma during the simulation. Because each impacting beam ion will stimulate the emission of many electrons, we also permit SCLE of electrons at the z = 100 cm wall. An electron trap prevents electrons from drifting upstream into the magnetic focusing region. The trap consists of a 1-cm-long ring electrode that is centered at z = -18.5 cm and negatively biased in the simulation at 1 kV. Finally, these PIC simulations are collisionless, with no beam stripping or ionization processes.

Non-neutralized transport

As a preliminary test of the NTX system, the beam was injected into a vacuum pipe without any neutralization. Figure 38 shows the measured beam profiles at 1 m downstream from the exit of the final focus system. The energy varies from 260 to 300 keV, and the beam is in good agreement with WARP simulations, also shown in the figure. We note that these experimental results were obtained using a sufficiently large beam pipe after final focus, ensuring that electron emission from the walls was negligible. Similar neutralization runs with the nominal 7-cm diameter beam pipe

initially showed much smaller spot sizes due to the capture of free electrons from the wall, but this anomalous behavior disappeared when the walls were screened by negatively charged mesh to trap these electrons.

Although the experimental focal spot is in good agreement with simulation results, a careful comparison of the radial density profiles shows qualitative differences. Figure 39 shows a comparison of profiles at the nominal focal point, 1m beyond last final-focus magnet. The experimental profile is hollow, and there is substantial charge in a halo extending well beyond the calculated 1.5-cm beam edge. In contrast, the LSP simulation gives a profile with negligible halo and a broad density peak at the beam center, providing that we ignore the statistically insignificant values within a 1-mm radius. The calculation uses the same initial emittance, radius, and convergence angle as the experiment, but it is idealized in assuming axisymmetry, neglecting interactions with the background gas, and specifying an initially Gaussian velocity distribution. To determine whether these idealizations account for the observed discrepancy, we need to initialize the simulations with a more-realistic phase-space distribution. The new optical diagnostic described in Section IIB will furnish the required data.

Neutralized transport

The low emittance ($\varepsilon_n \sim 30$ mm-mr) of the beam at the entrance to the neutralized region allows for the beam to be focused to a small spot size (1-2 mm radius) at the focal point for neutralized ballistic transport. Figure 40 shows the experimental dependence of beam focal-spot size on neutralization mechanism.

LSP simulations of NTX including plasma plug and volumetric neutralization were performed starting from beam initial conditions at the entrance to the neutralization region. In one series of LSP simulations, shown in Fig. 41, the initial condition is the final phase-space distribution as calculated by WARP for the transport of the NTX beam from the gun to the exit of the final focus system. There is qualitative agreement with measured spot sizes, but a detailed measurement of the 4-D phase-space distribution at the exit of the final-focus section is essential in order to initialize more-realistic simulations of NTX neutralized beam transport.

A series of idealized axisymmetric LSP simulations indicates that plasma neutralization should be fairly insensitive to variations in plasma parameters. These simulations use an idealized Gaussian velocity distribution, with the same emittance used above. A comparison between experiment and theory of the radial distribution profile at focus is shown in Fig. 42. The basic size of the beam spot is similar in both cases with differences attributed to a halo due to nonlinear focusing seen in the experimental curve. Simulations show that if electrical connection is maintained to the chamber wall through electron SCLE, the beam spot shows little variation for plasma densities ranging from 3×10^8 - 3×10^{10} cm^{-3} for an initial plasma temperature of 3-eV. Without electron emission from the wall, the plasma plug charged up due to loss of electrons and the spot size degraded in time, particularly for smaller plasma densities. For a 6-eV initial plasma temperature, which is greater than $\frac{1}{2}m_e v_i^2$, the beam spot size was roughly 50% larger than the case with a 3-eV plasma. The sensitivity of the beam spot to incoming beam

emittance is calculated to be weak with only a 30% spot-size variation for a factor of three change in emittance. This low sensitivity to emittance indicates that charge neutralization in the NTX experiment should be quite close to that 96% value seen in simulations and not influenced by details in the emittance.

"Analog simulation" of fully neutralized beam transport

As discussed in Section IIIB, we are developing an optical technique to measure the 4-D phase-space distribution of the beam. The phase space distribution $f(x,y,x',y')$ is measured by scanning the beam with a 0.05-cm diameter pinhole and letting the transmitted beamlet travel about 1 m before striking the scintillator. The pinhole position defines the coordinates x and y, and from the image, we can extract the density distribution of x' and y'. This technique will be used to measure the detailed structure of the phase space distribution.

The same diagnostic system can be used to simulate the effect of full neutralization on a beam, since each beamlet going through a pinhole only carries the information about the phase space distribution at a given location without being perturbed by the space charge of the full beam. The superposition of all the pinhole images at a given location can be compared with a beam-transport calculation where the space charge is turned off at the pinhole-scan plane. Figure 43 shows a comparison between this "analog simulation" and a WARP run with the space-charge field artificially suppressed. The agreement of the focal-spot radius is seen to be excellent, despite differences in azimuthal structure. This agreement indicates that the NTX emittance is low enough after focusing to produce a focal spot of about 1 mm radius, given adequate neutralization.

VI. Summary

The Neutralized Transport Experiment at LBNL is providing the first experimental validation of neutralized ballistic transport of a space-charge-dominated beam. Although the experiment uses a beam that is orders of magnitude lower in current than driver for heavy-ion fusion, a careful choice of parameters guarantees that the transport physics closely matches that of a full-scale system. To date, beam-transport experiments through the NTX final focus-systems have produced high-perveance beams with the emittance and convergence angle needed for chamber-transport experiments. The first of these experiments have demonstrated dramatically improved focusing by passing the beam through a low-density plasma produced by a metal-arc source, and forthcoming tests will study the effects of a second plasma near the beam waist, mimicking the effects of a photoionized plasma near the fusion target. We are presently beginning a careful comparison of the experimental findings with the results of numerical simulations.

In parallel to the transport experiments, we are developing two new diagnostic tools. The first, a refinement of the conventional "pepper-pot" imaging technique, gives a detailed time-resolved view of the beam 4-D transverse phase space for beams that have good pulse-to-pulse reproducibility. Using this technique to map the 4-D phase-space distribution at the exit of the NTX final-focus system will provide initial conditions for realistic simulations of the neutralized-transport experiments. The other tool is a non-

intercepting diagnostic that uses a low-energy electron beam directed across the NTX beam line to map out the transverse charge distribution of the ion beam. Both diagnostic techniques provide new information about the structure of the NTX beam and will facilitate our understanding of neutralization physics.

Acknowledgments

This work was performed under the auspices of the US Department of Energy by University of California Lawrence Livermore National Laboratory and Lawrence Berkeley National Laboratory under Contracts No. W-7405-ENG-48 and DE-AC-3-76SF00098, and by Princeton Plasma Physics Laboratory under contract DE-FG-0295ER40919.

References

[1] S. S. Yu, W.R. Meier, R.P. Abbott, J.J. Barnard, T. Brown, D.A. Callahan, P. Heitzenroeder, J.F. Latkowski, B.G. Logan, S.J. Pemberton, P.F. Peterson, D.V. Rose, G.-L. Sabbi, W.M. Sharp, and D.R. Welch, "An Updated Point Design for Heavy Ion Fusion," *Proc. 2002 Amer. Nucl. Soc. Fusion Topical Meeting*, 17-21 November 2002, Washington, DC (to be published).
[2] W. B. Herrmannsfeldt, "Final Focusing and Transmission to Target," ERDA Summer Study for Heavy Ions for Inertial Fusion, LBL-5543 (1976), p. 25.
[3] S. S. Yu, H. L. Buchanan, E. P. Lee, and F. W. Chambers, "Beam Propagation through a Gaseous Reactor," Proc. 1978 Heavy Ion Fusion Workshop, Argonne National Laboratory Report ANL-79-41 (1979), p. 403.
[4] C. L. Olson, "Final Transport in Gas and Plasma," Proc. 1979 Heavy Ion Fusion Workshop, Lawrence Berkeley Laboratory Report LBL-10301 (1980), p. 403.
[5] B. Badger, *et al*., "HIBALL-II – An Improved Conceptual Heavy Ion Beam Driven Fusion Reactor Study," University of Wisconsin Report UWFDM-625 (1984).
[6] S. A. MacLaren, "A Scaled Final Focus Experiment for Heavy Ion Fusion," PhD Thesis, University of California Berkeley (2000).
[7] W. M. Sharp, D. P. Grote, D. A. Callahan, M. Tabak, E. Henestroza, S. S. Yu, P. F. Peterson, D. R. Welch, and D. V. Rose, "Realistic Modeling of Chamber Transport for Heavy-Ion Fusion," *Proc. 2003 Part. Accel. Conf.,* 12-16 May 2003, Portland, OR (to be published).
[8] J. Lindl, *Plasma Phys.* **2**, 3933 (1995)
[9] R. W. Moir, R. L. Bieri, X. M. Chen, T. J. Dolan, M. A. Hoffman, P. A. House, R. L. Leber, J. D. Lee, Y. T. Lee, J. C. Shrock, M. T. Tobin, and W. H. Williams, *Fusion Technol.* **25**, 5 (1994).
[10] M. Tabak and D. A. Callahan-Miller, *Nucl. Instr. and Meth in Phys. Res. A* **415**, 75 (1998).
[11] D. A. Callahan-Miller and M. Tabak, *Nucl. Fusion* **39**, 1547 (1999).
[12] T. P. Hughes, *et al*., *Phys. Rev. ST Accel. Beams* **2** (1999) 110401.
[13] D. R. Welch, *et al*., *Nucl. Instrum. Meth. Phys. Res A* **464**, 134 (2001).
[14] W. M. Sharp, *et al*., "Realistic Modeling of Chamber Transport for Heavy-Ion Fusion," *Proc. 2003 Particle Accel. Conf.*, 12-16 June 2003, Portland, OR (to be published).

[15] D. P. Grote, A. Friedman, I. Haber, and S. S. Yu, *Fusion Eng. Design* **32-33**, 133 (1996).
[16] J. D. Lawson, *J. Electron. Control* **5**, 146 (1958).
[17] M. Reiser, *Theory and Design of Charged Particle Beams* (John Wiley & Sons, New York, 1994), p. 57-59.
[18] D. A. Callahan, *Fusion Eng. Des*. **32–33**, 441 (1995).
[19] N. Barboza, *Fusion Eng. Des.* **32–33**, 453 (1995).
[20] W. M. Sharp, D. A. Callahan-Miller, A. B. Langdon, M. S. Armel, and J.-L. Vay, *Nucl. Instrum. Methods Phys. Res. A* **464**, 284 (2001).
[21] D. V. Rose, D. R. Welch, B. V. Oliver, W. M. Sharp, and A. Friedman, *Nucl. Instrum. Methods Phys. Res. A* **46**4, 299 (2001).
[22] I. D. Kaganovich*, et al., Phys. .Plasmas* **8,** 4180 (2001).
[23] D. R. Welch, D. V. Rose, W. M. Sharp, and S. S. Yu, *Laser Part. Beams* **20**, 621(2003*)*.
[24] W. M. Sharp, D. A. Callahan, M. Tabak, S. S. Yu, and P. F. Peterson, *Phys. Plasmas* **10**, 2457 (2003).
[25] W. M. Sharp, *et al*., *Fusion Sci. and Tech*. **43**, 39*3* (2003).
[26] W. M. Fawley, T. Garvey, S. Eylon, E. Henestroza, T. J. Fessenden, K. Hahn, L. Smith, and D. P. Grote, *Phys. Plasmas* **4**,880 (1997).
[27] S. Eylon, E. Henestroza, P. K. Roy, and S. S. Yu, "High brightness potassium source for the HIF neutralized transport experiment", *Proc. 2003 Particle Accel. Conf.*, 12-16 June 2003, Portland, OR (to be published).
[28] E. Henestroza, F. M. Bieniosek, S. Eylon, P. K. Roy, and S. S. Yu, "Final Focus System for High Intensity Beams," *Proc. 2003 Particle Accel. Conf.*, 12-16 June 2003, Portland, OR (to be published).
[29] E. Henestroza, F. M. Bieniosek, S. Eylon, P. K. Roy, and S. S. Yu, "Neutralized Transport of High Intensity Beams", *Proc. 2003 Particle Accel. Conf.*, 12-16 June 2003, Portland, OR (to be published).
[30] D. Baca, J. W. Kwan, J. K. Wu, and E. Chacon-Golcher, "Fabrication of Large Diameter Alumino-Silicate K^+ Sources," *Proc. 2003 Particle Accel. Conf.*, 12-16 June 2003, Portland, OR (to be published).
[31] S. Eylon, "Multiple Heavy Ion Beams Induction Linac Experiment," *AIP Conf. Proc. 252,* W. Berry and P. Kloeppel, eds. (New York, American Institute of Physics, 1991), p.225.
[32] M. J. Rhee and R. F. Schneider, *Part. Accel.* **20**, 133 (1986).
[33] L. Ahle and H. S. Hopkins, "Gated Beam Imager for Heavy Ion Beams," Proc. 1998 Beam Instrumentation Workshop, 4-7 May 1998, Palo Alto, CA (1998).
[34] P. K. Roy, S. S. Yu, J. Judvig, D. B. Shuman, S. Eylon, E., Henestroza, W. G. Greenway, D. L. Vanecek, W. L. Waldron, and R. Hannik, "Design and Development of an Electron Beam Diagnostic System for Non-Perturbative Space-Charge Measurements on an Ion Beam," submitted to *Rev. Sci. Instru.* (2003).
[35] M. Reiser, *op. cit*., p. 61.
[36] C. Lejeune and J. Aubert, *Applied Charged Particle Optics, Advances in Electronics and Electron Physics,* Supplement 13A, A. Septier, ed. (Academic Press, San Diego, 1980), p. 159-259.

[37] W. B. Herrmannsfeldt, “EGUN – An Electron Optics and Gun Design Program,” SLAC-Report 331 (1988).
[38] M. Reiser, *op. cit*., p. 45-46.
[39] D. Neuffer, “Geometric aberrations in final focusing for heavy ion fusion”, *Proc. 1978 HIF Workshop*, 19-26 September 1978, Argonne, IL,Argonne National Laboratory Report ANL-79-41 (1978).
[40] D. B. Shuman, E. Henestroza, D.L. Vanecek, W.L. Waldron, S.S. Yu, “A Large Bore Pulsed Quadrupole Magnet for Transport of High Current Beams at Low Energies,” Proc. 2001 Particle Accel. Conf., 18-22 June 2001, Chicago, IL (2001), p. 2935.
[41] R. A. MacGill, M. R. Dickinson, A. Anders, O. R. Monteiro, and I. G. Brown, “Streaming metal plasma generation by vacuum arc plasma guns,” *Rev. Sci. Instrum.* **69**, 801 (1998).
[42] A. Anders, *Surf. Coat. Technol.* **120-121**, 319 (1999).
[43] A. Anders and G. Y. Yushkov, J. App;. Phys. 92, 4824 (2002).

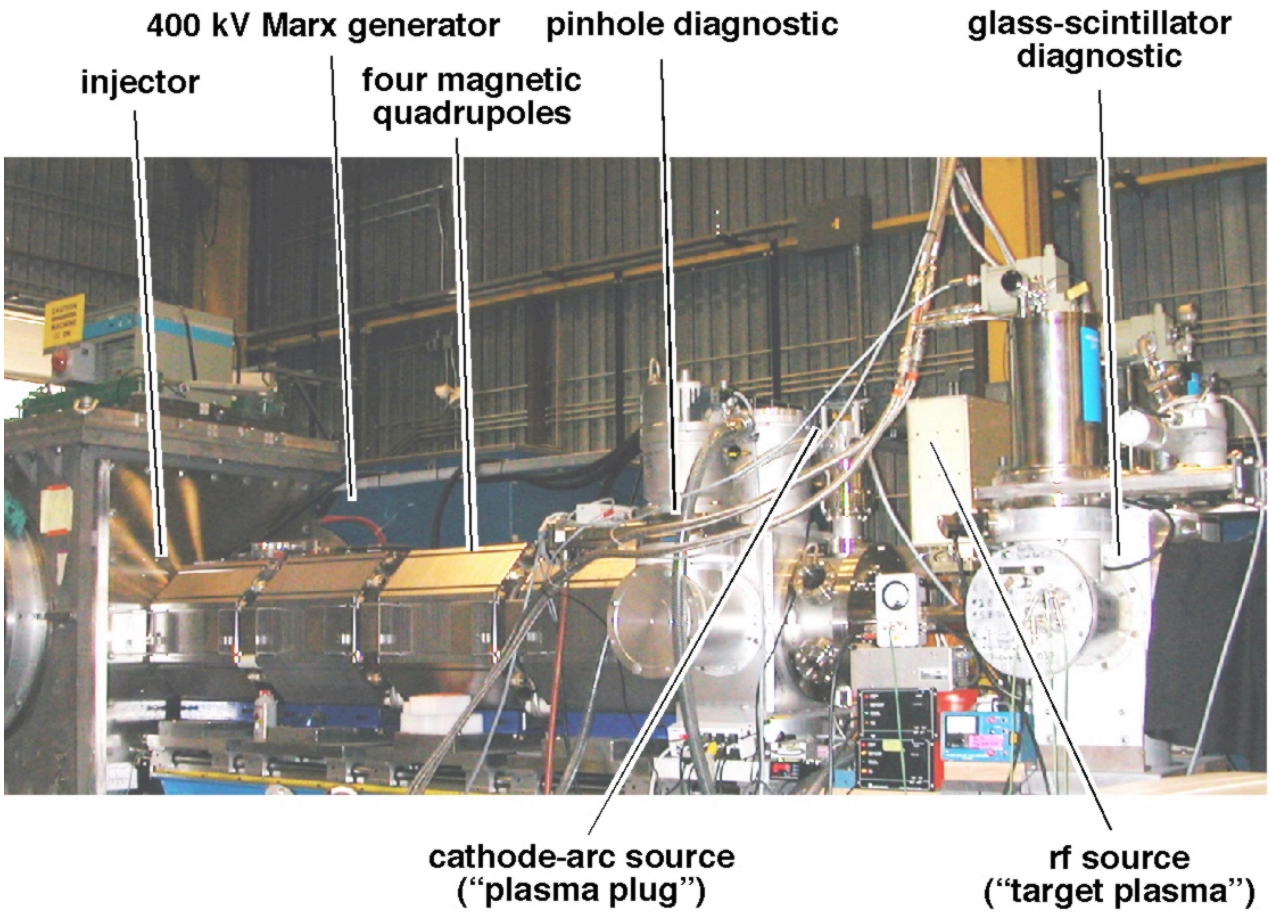

Figure 1. Photograph of the Neutralized-Transport Experiment (NTX).

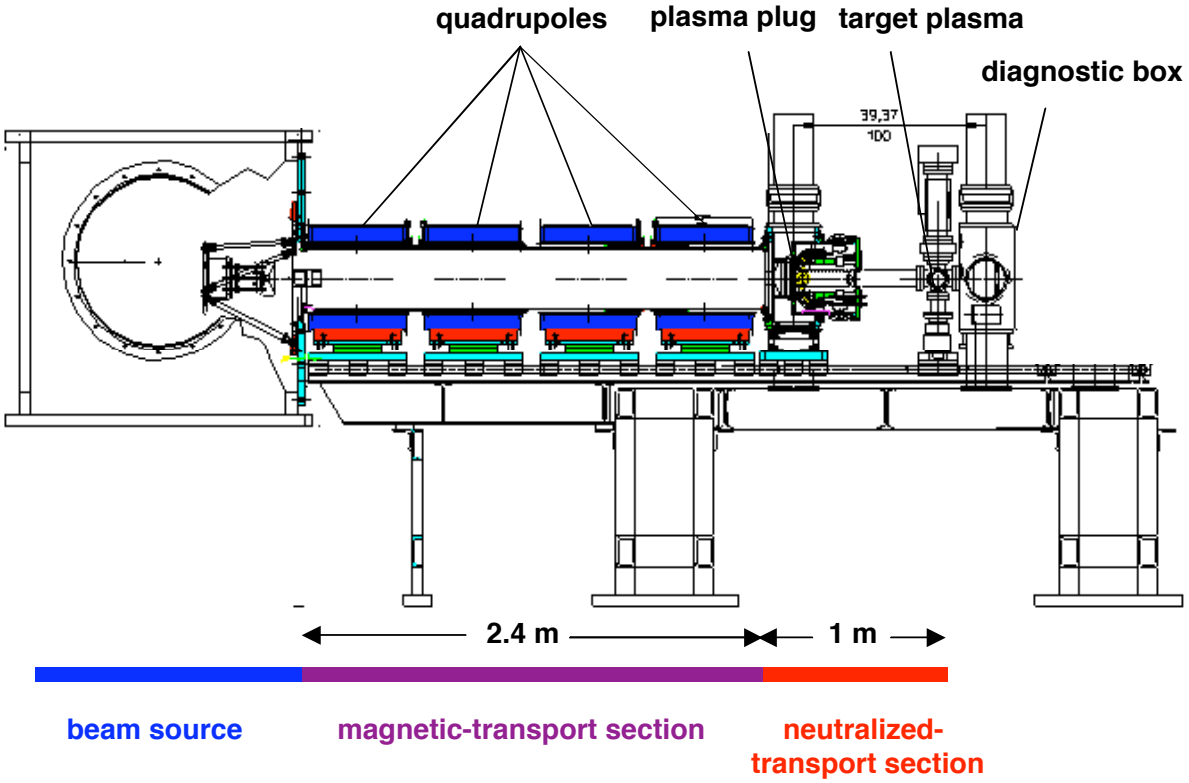

Figure 2. Plan view of NTX injector, magnetic transport, and neutralized-transport sections. The Marx generator, located to the side of the experiment, is not shown.

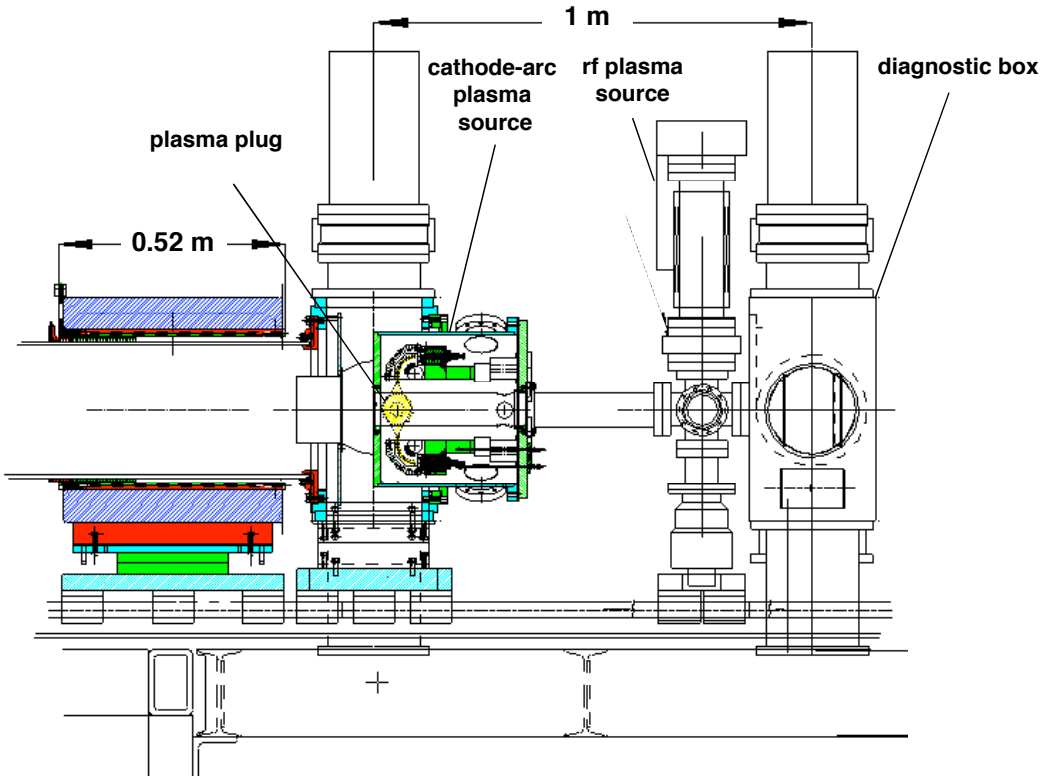

Figure 3. Plan view of the NTX neutralization section.

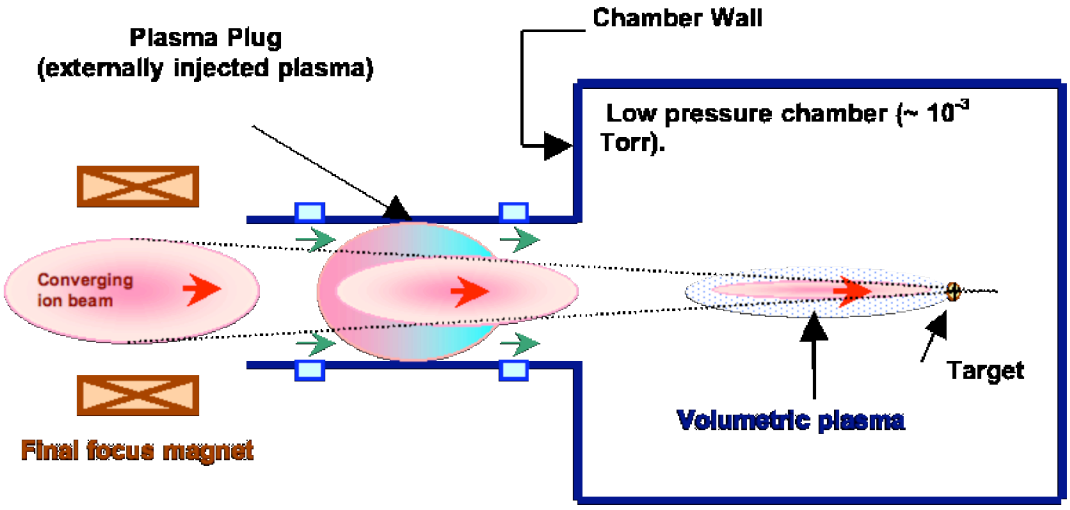

Figure 4. Generic layout of a plasma-neutralization system.

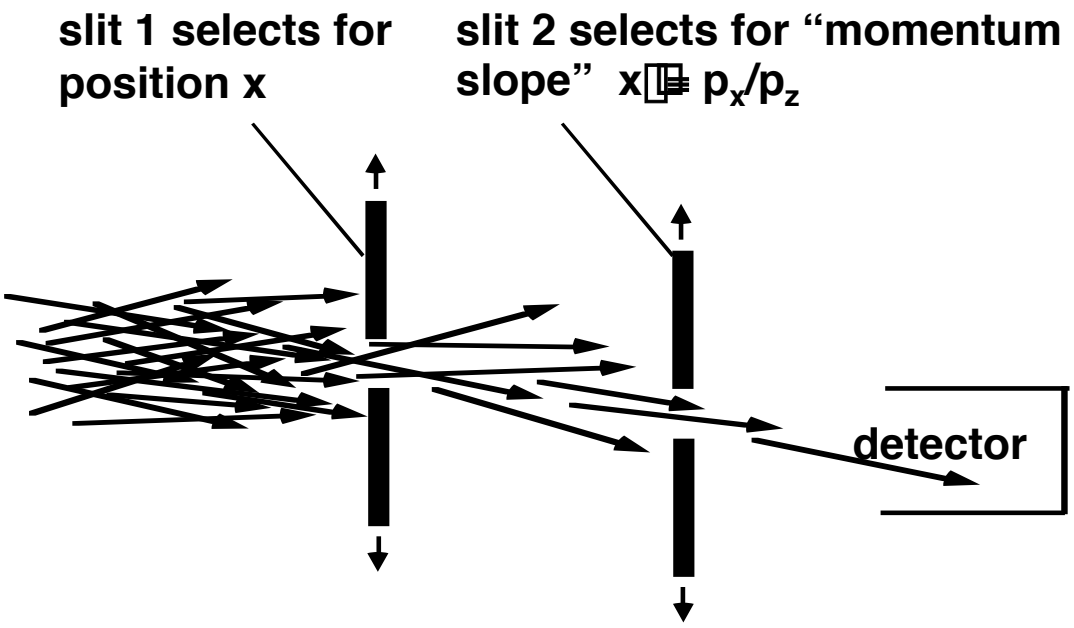

Figure 5. Sketch of a two-slit technique for mapping the (x, x’) phase space of a beam.

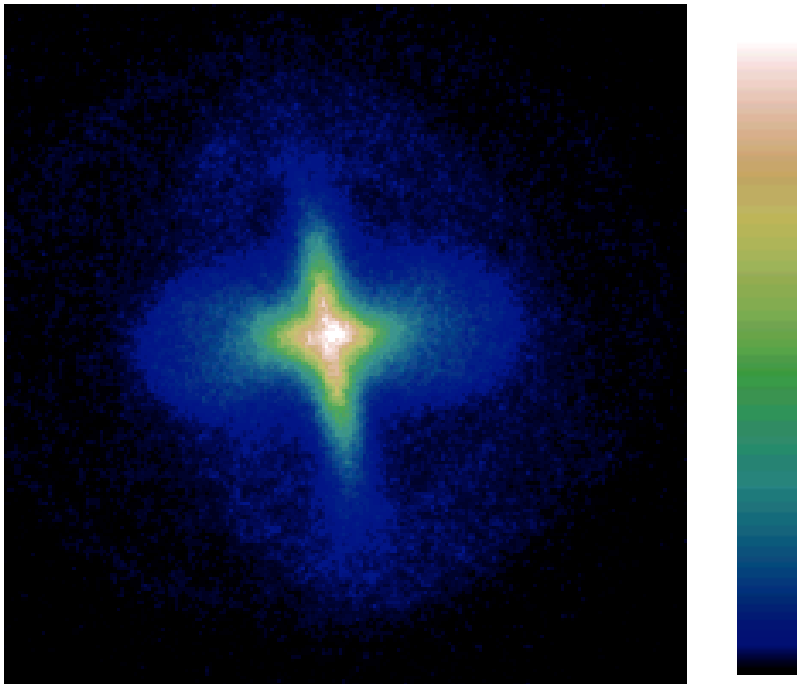

Figure 6. Transverse beam image taken on NTX. The scale is 3-cm x 3-cm. The color palette used to represent the images is shown at the right.

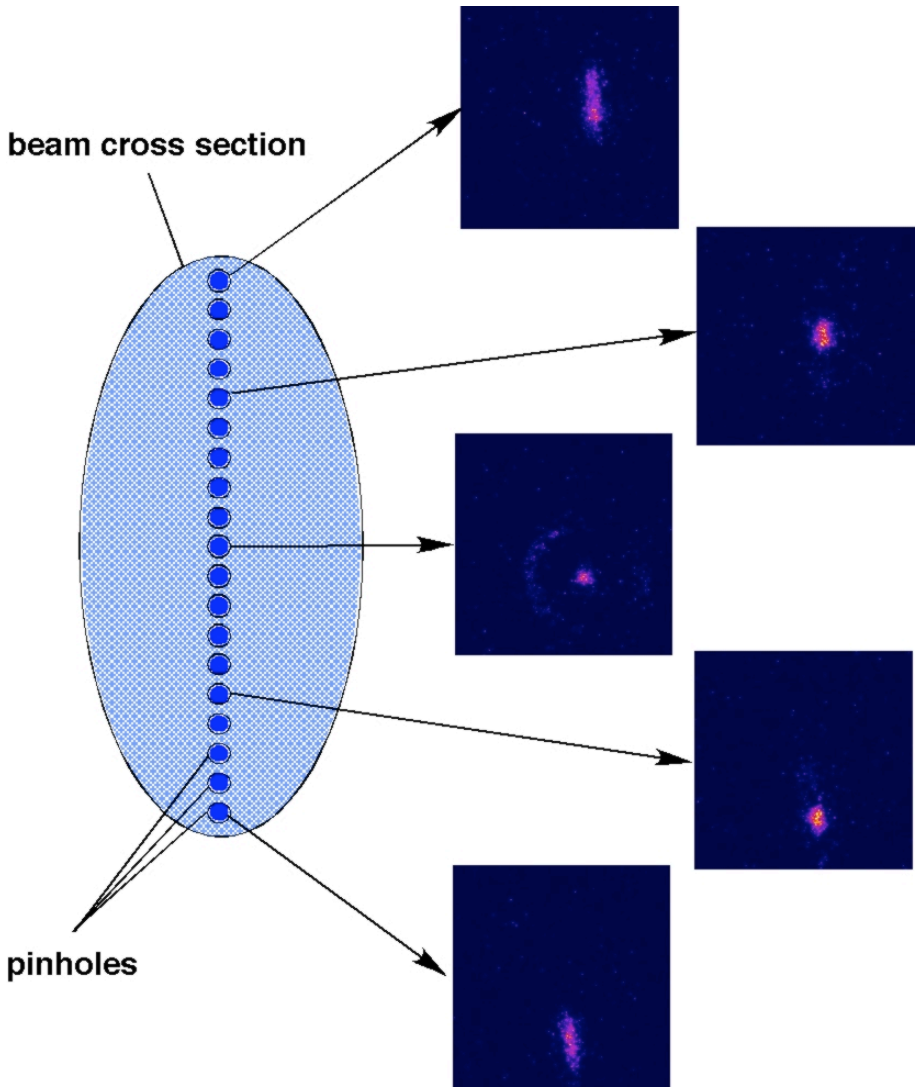

Figure 7. Beam imaging technique to measure the phase-space distribution *f(x,y,x´,y´)*.

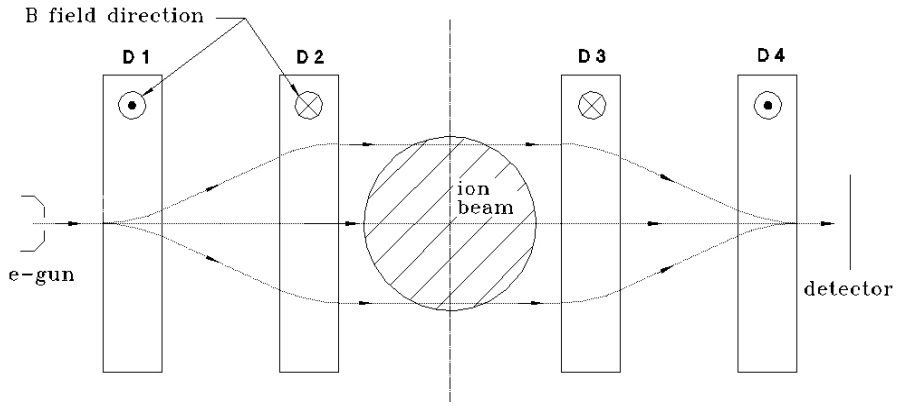

Figure 8. Sketch of the NTX non-intercepting beam diagnostic.

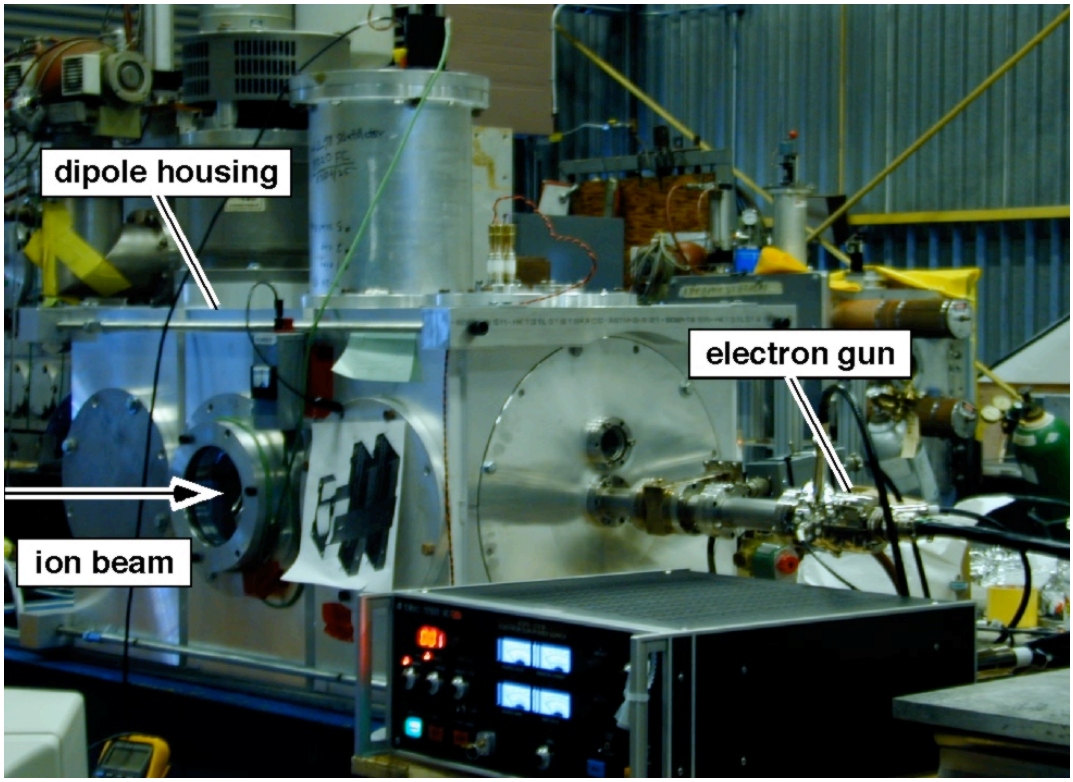

Figure 9. Photograph of the NTX non-integcepting beam diagnostic.

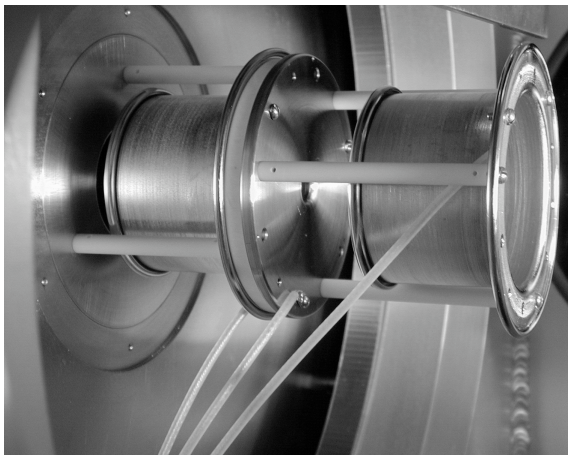

Figure 10. Photograph of the NTX beam scraper system.

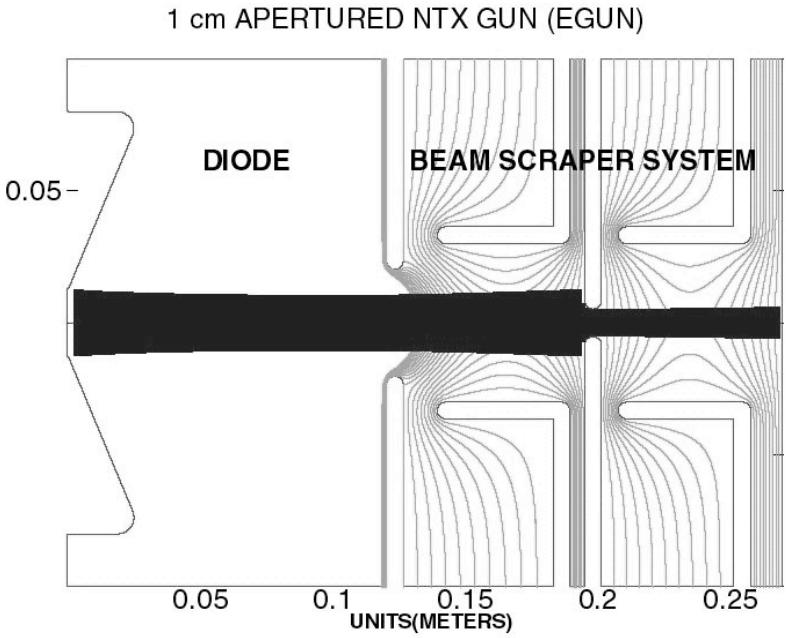

Figure 11. EGUN simulation of the NTX diode and beam aperture.

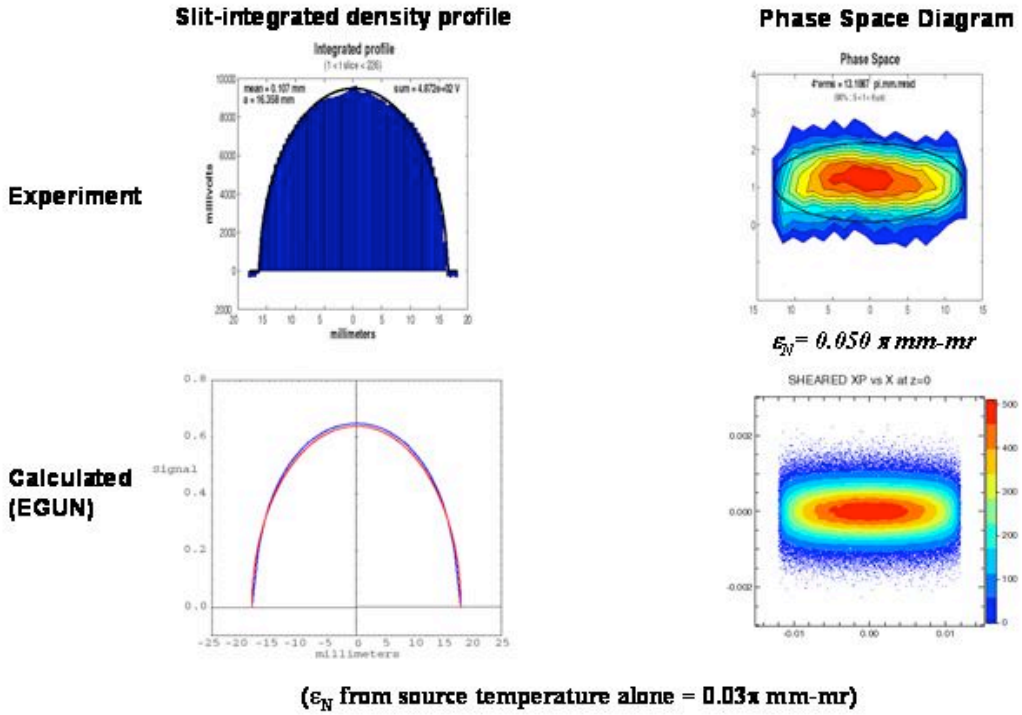

Figure 12. Slit-integrated density profile and (x, x') phase space of a high-brightness apertured beam (300kV, 25 mA, 2-cm aperture). The corresponding EGUN calculations are shown below the measurements

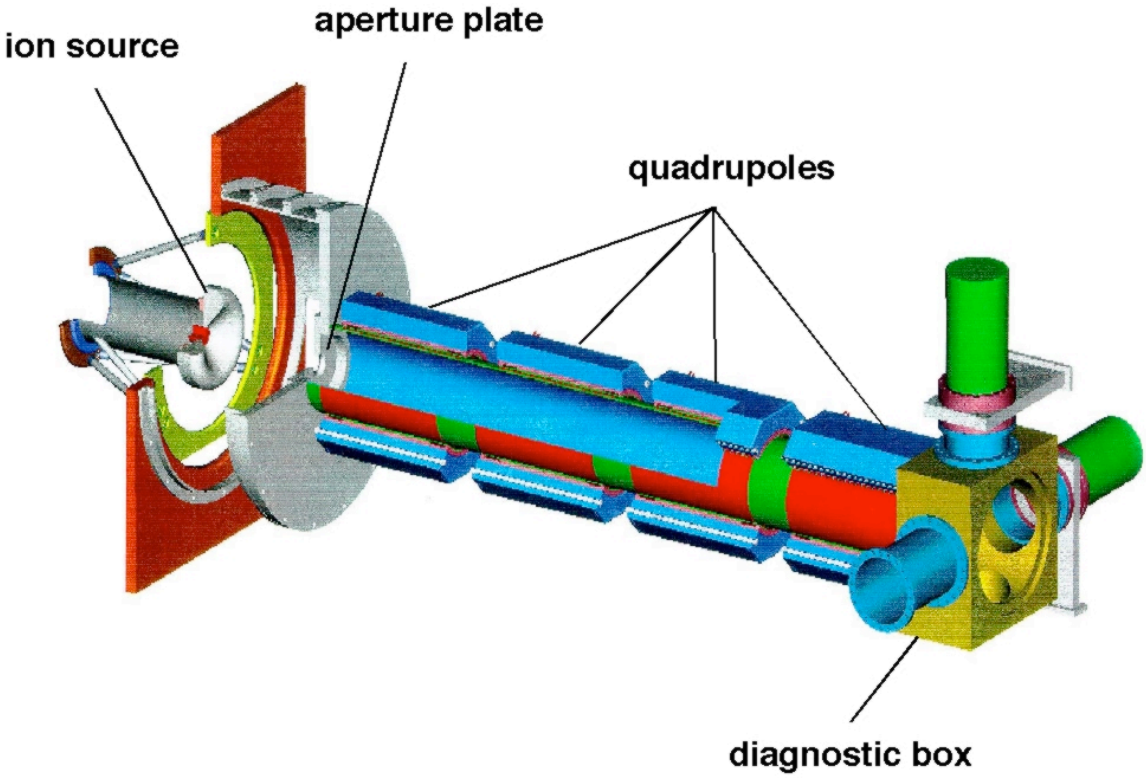

Figure 13. NTX injector and magnetic final-focus lattice with selected areas cut away to reveal interior components.

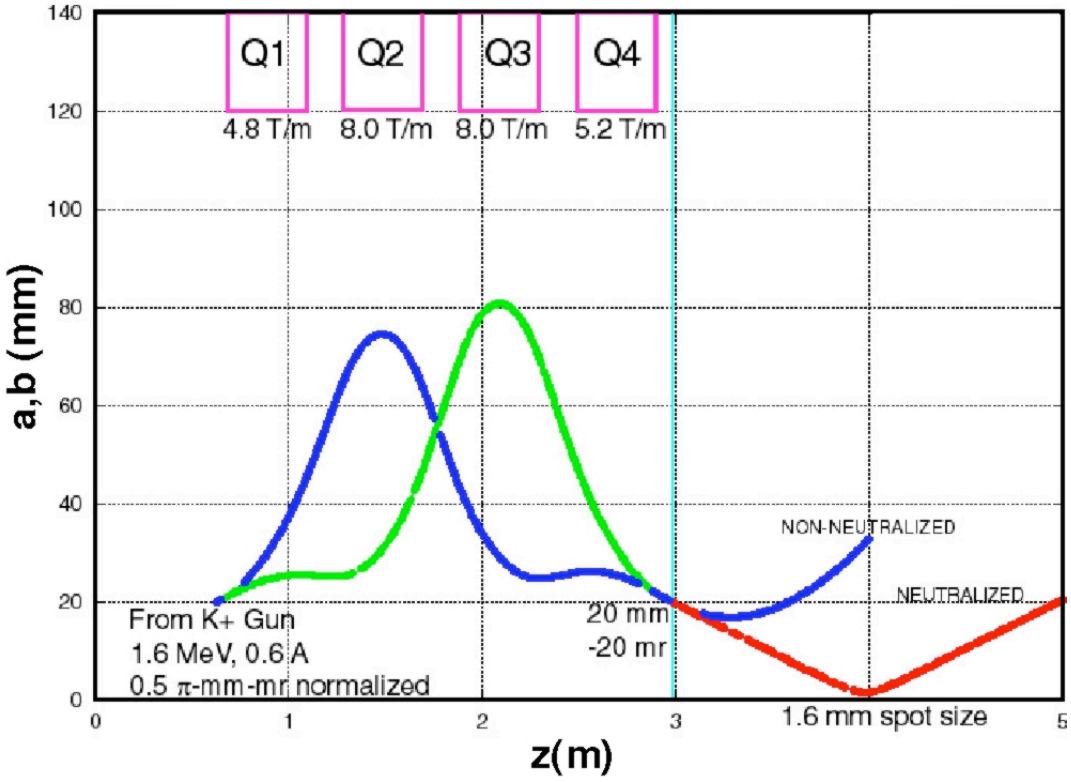

Figure 14. Envelope simulation of transport in NTX magnetic lattice.

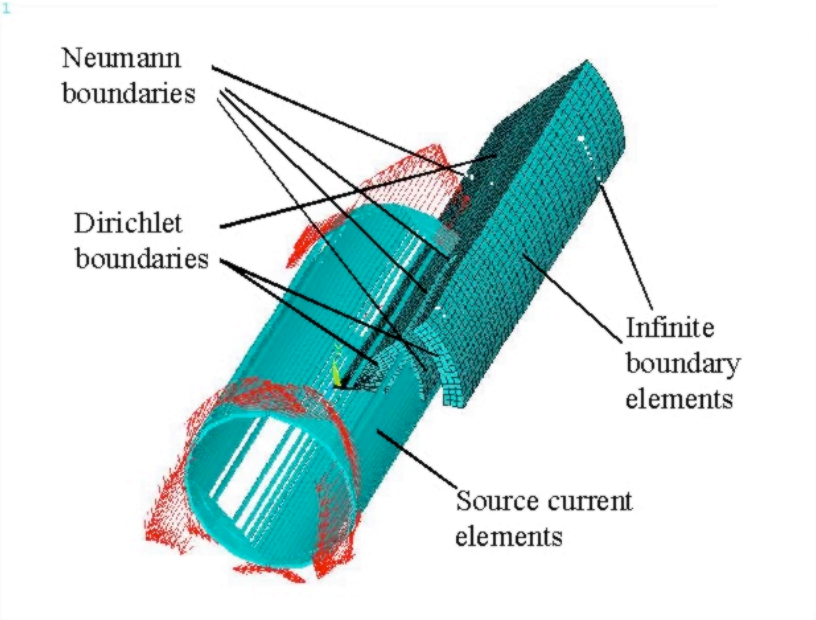

Figure 15. Symmetrical magnet model with half octant shown.

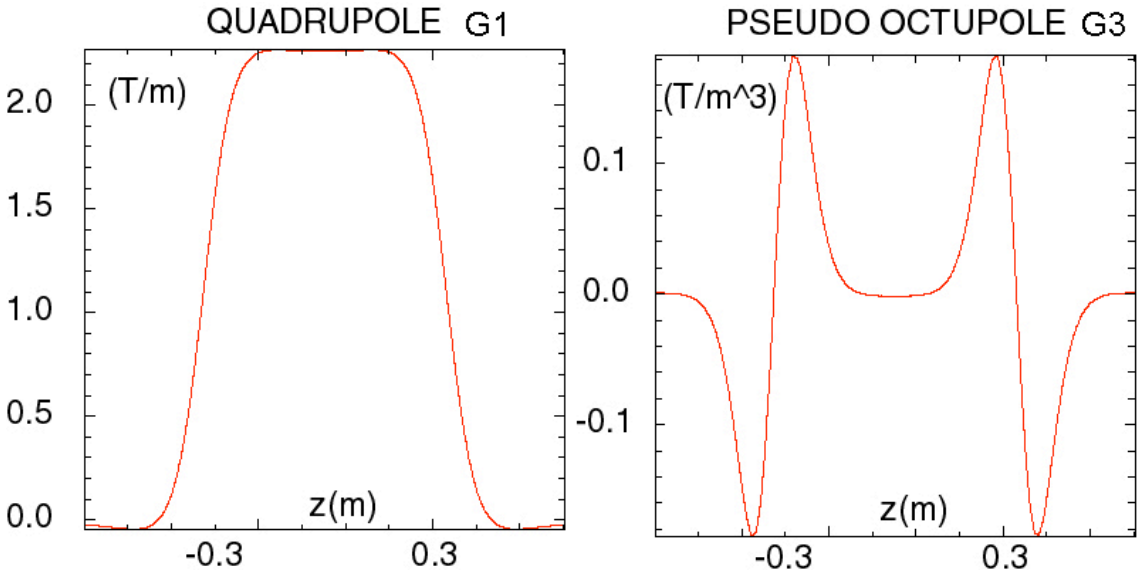

Figure 16. Dominant coefficients for the multipole decomposition

$$B_{\square}(r,\square,z) = G_1(z)r\cos(2\square) + G_3(z)r^3\cos(2\square) + \ldots$$

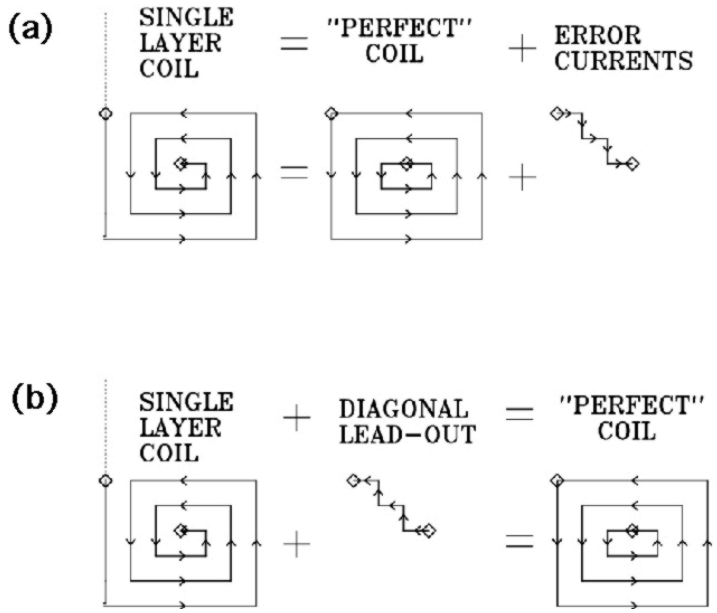

Figure 17. Concept for correcting coil-winding errors. (a) Single-layer coil normally introduces error currents due to incomplete current loops. (b) Adding a diagonal lead-out can correct this problem and produce nearly perfect fields.

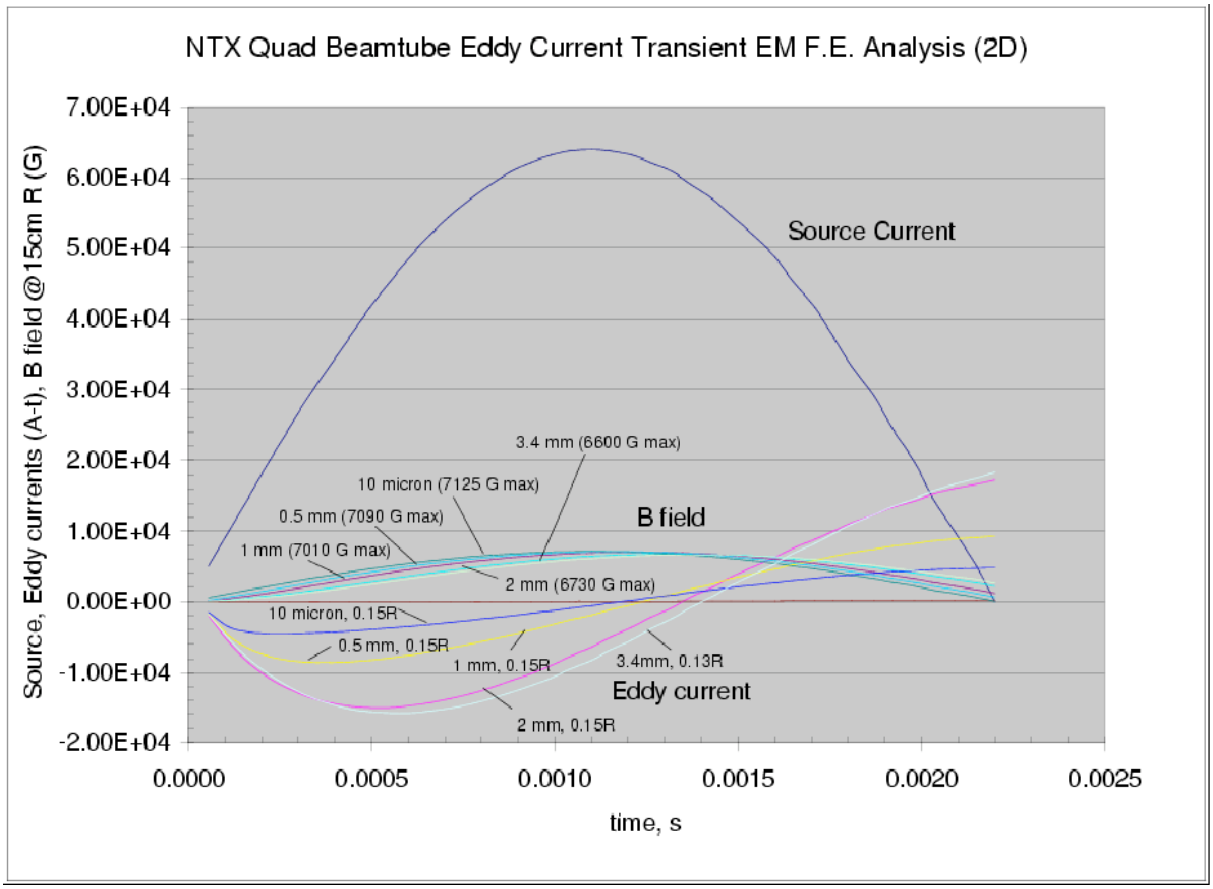

Figure 18. NTX beam-pipe eddy currents and magnetic fields.

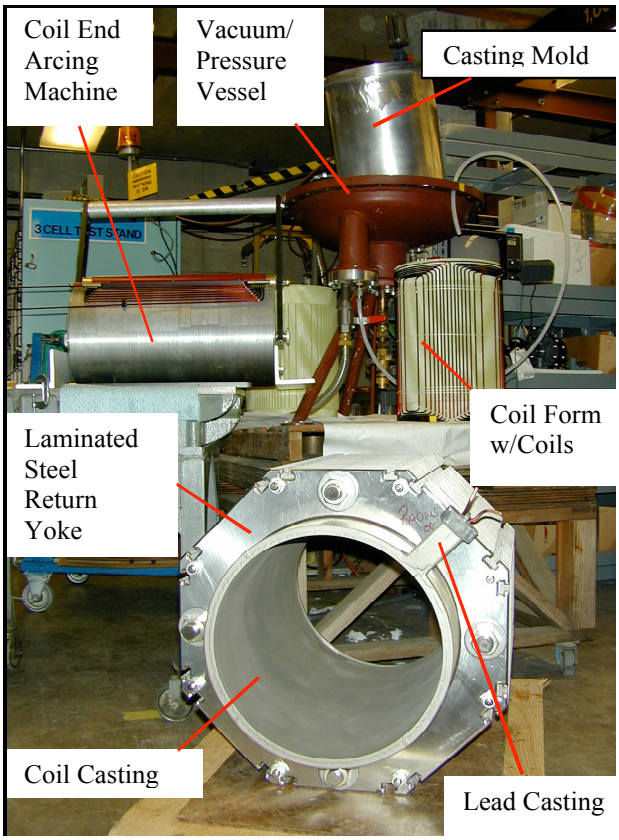

Figure 19. Photograph of an NTX magnet during fabrication.

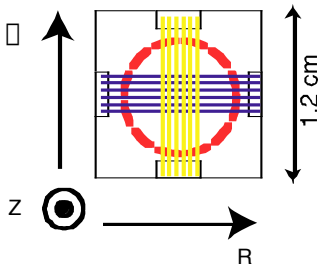

Figure 20. Illustration of the orientation of the windings on the magnetic-field probe. All windings have circular cross sections and consist of two layers

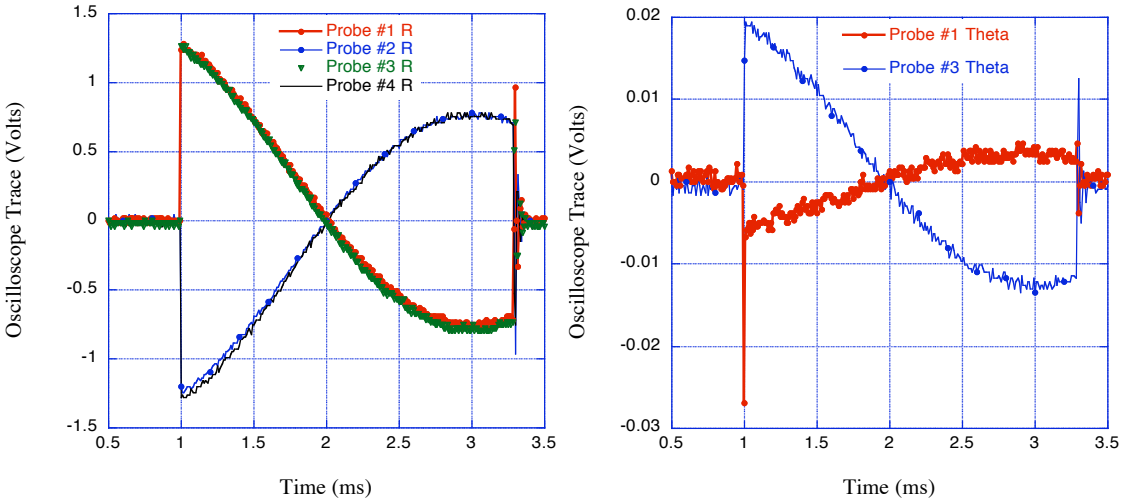

Figure 21. Oscilloscope traces of the probe output when the supporting cylinder is rotated to place probes at center of the quadrupole windings. The left traces are from loops oriented to sense radial flux, and the right traces are from loops sensing azimuthal flux.

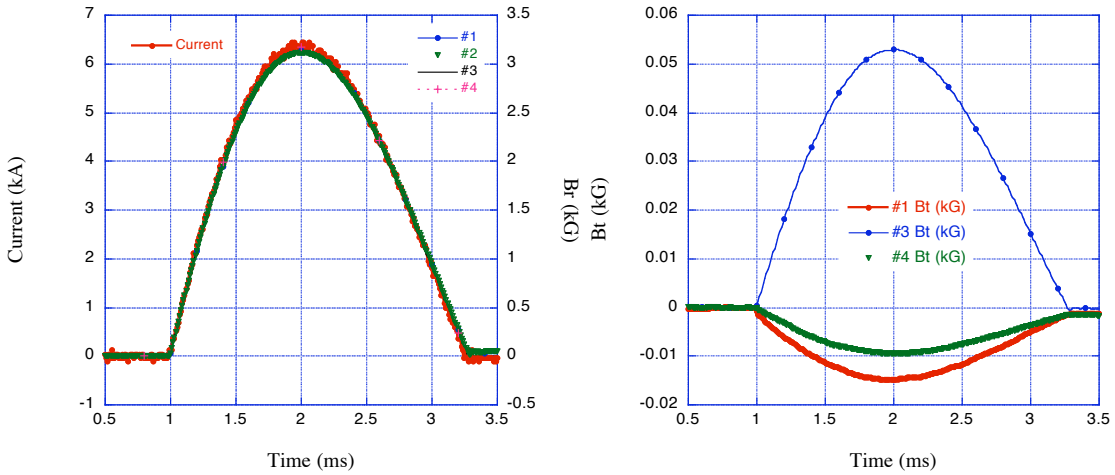

Figure 22. Magnet current along with the intergrated and calibrated radial field (left), and the corresponding azimuthal field (right).

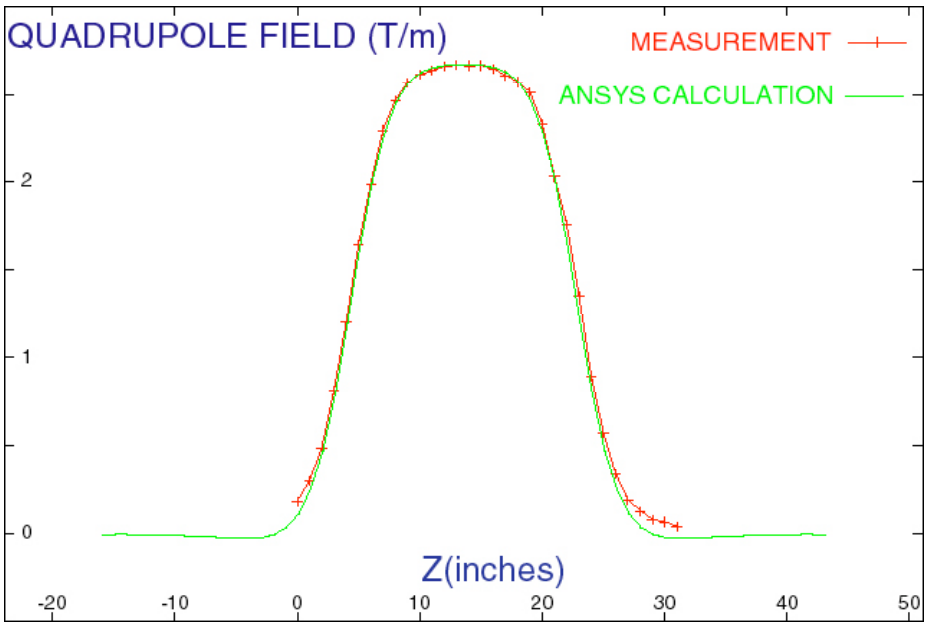

Figure 23. Calculated and measured NTX quadrupole gradients.

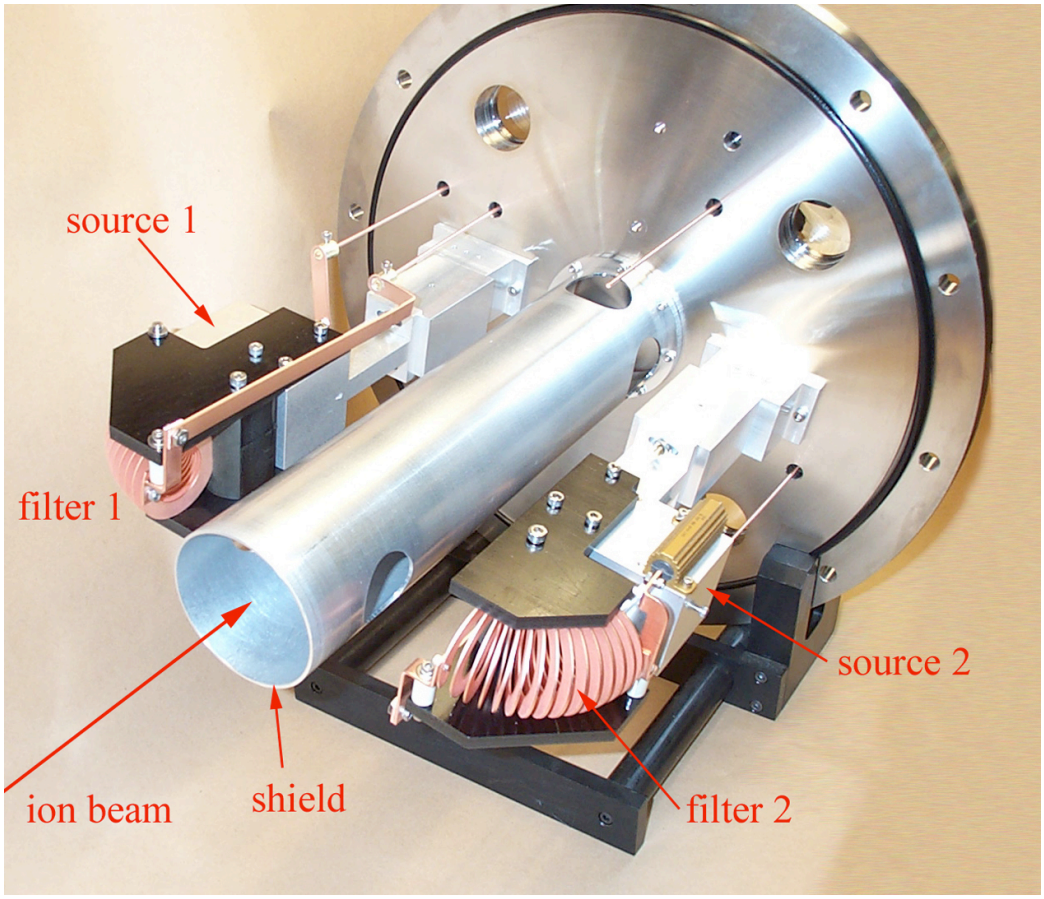

Figure 24. NTX cathode-arc plasma sources mounted on beam pipe. Plasma is injected in the path of the ion beam through openings in the aluminum metal shield. The shield is designed to reduce the magnetic field at the location of the ion beam, to limit plasma entering the quadrupole region, and to prevent source debris from entering the beam region.

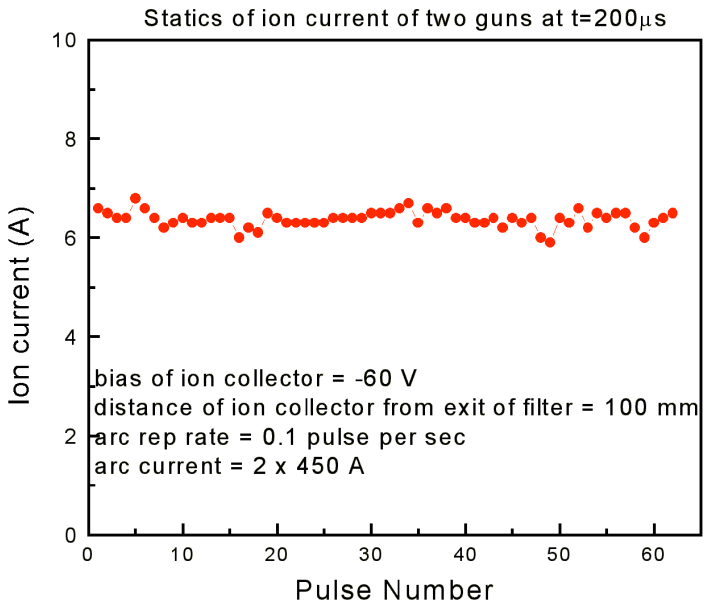

Figure 25. Ion current signal from the two cathode-arc plasma sources, each operating with 450 A arc current and fed by the same pulse-forming network.

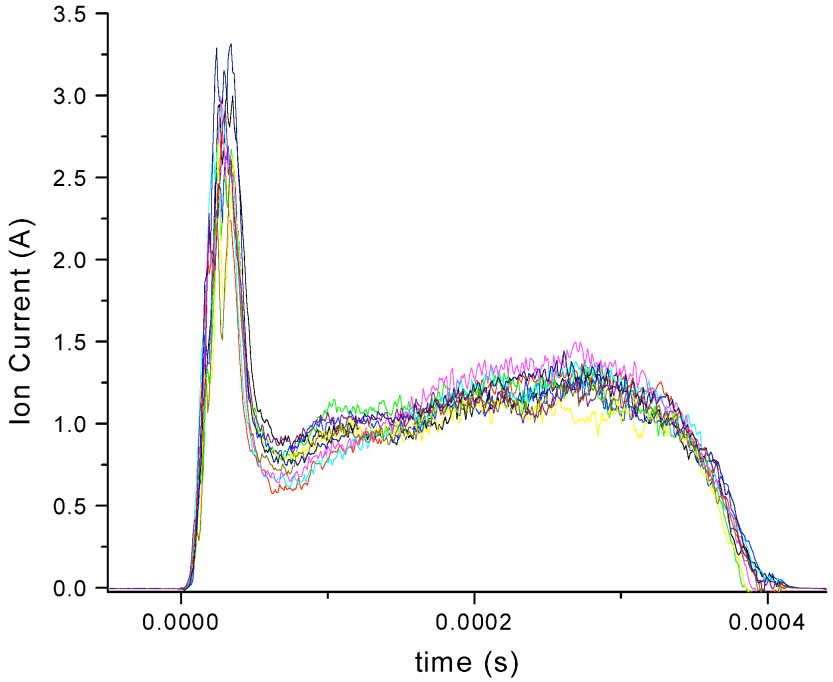

Figure 26. Aluminum ion current of ten successive arc pulses collected by an ion collector at the location of the NTX ion beam.

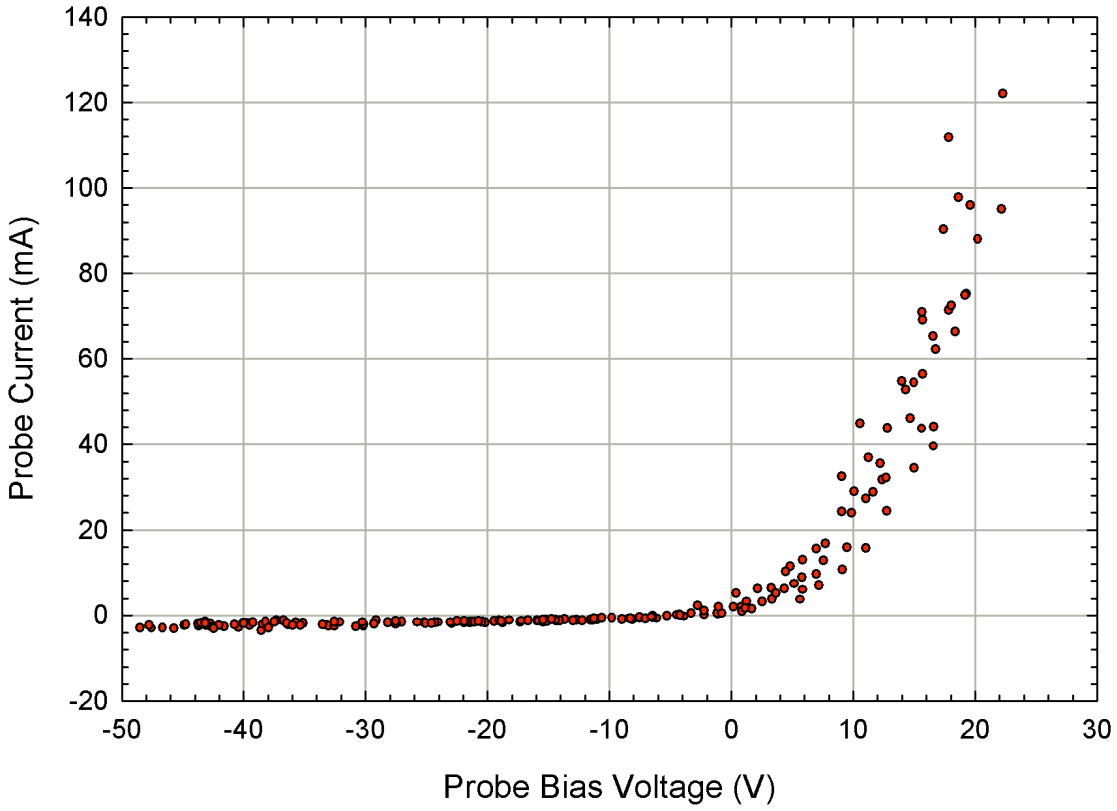

Figure 27. Each point on the IV characteristic is taken from a single shot of the cathode-arc plasma source. The shot-to-shot variability produces a spread in the data. The ion saturation current can be used to determine the plasma density.

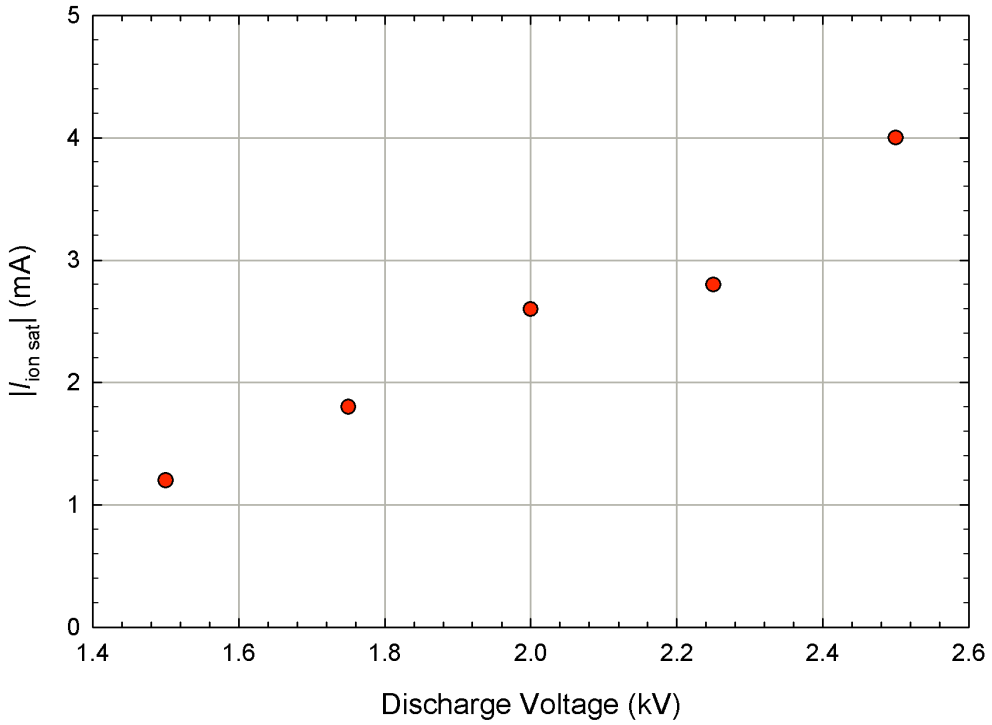

Figure 28. Ion saturation current as a function of NTX cathode-arc dischage voltage. The plasma density varies proportionally with this current.

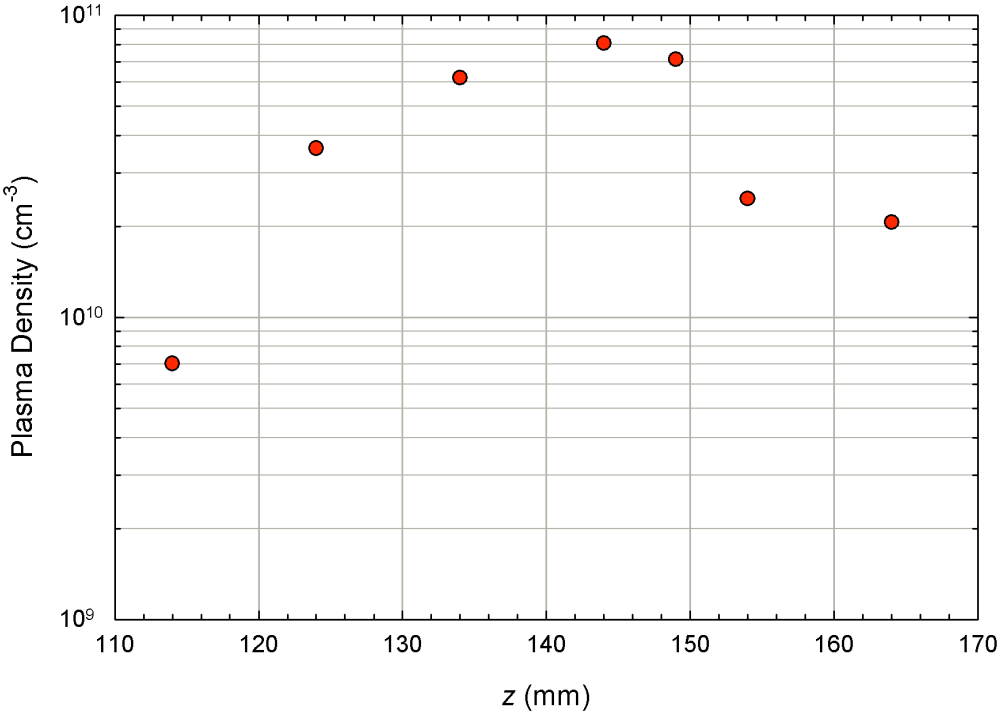

Figure 29. Axial profile of the plasma density as a function of longitudinal position near the plasma entry ports.

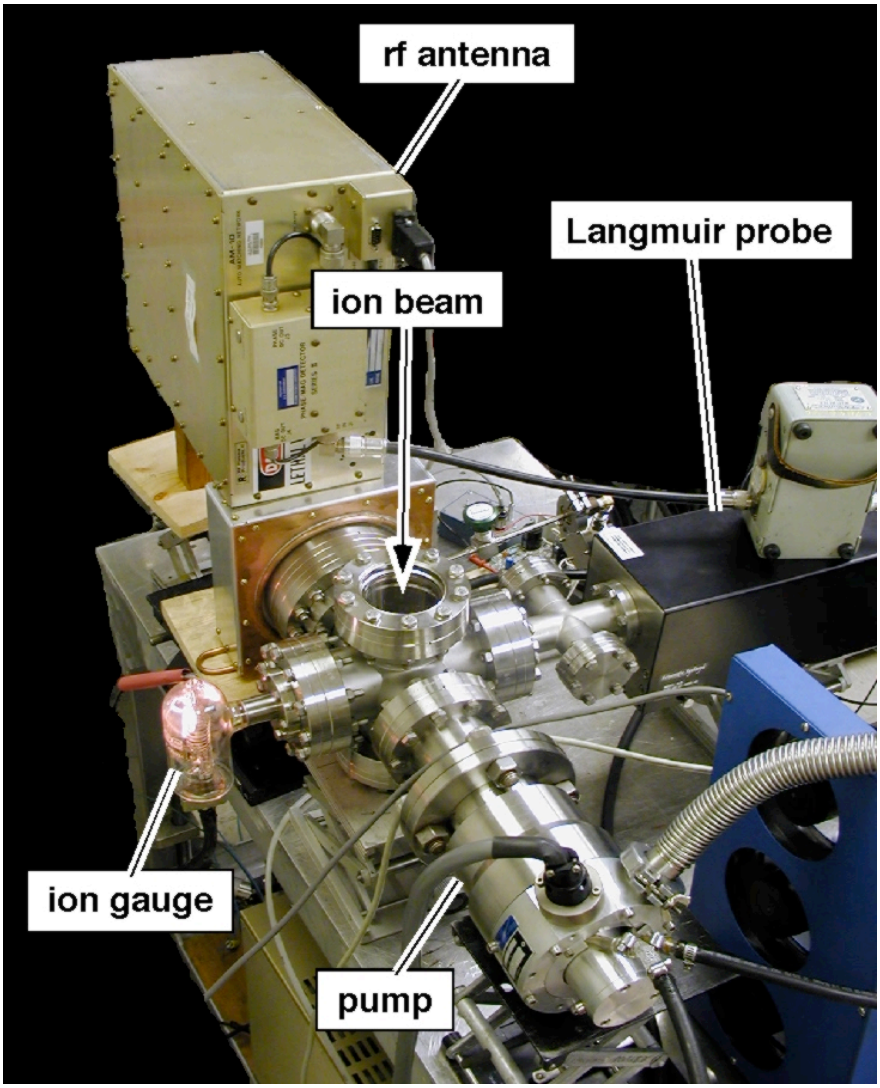

Figure 30. PPPL rf Argon plasma source before installation. Plasma is created in the six-way cross along the ion-beam path.

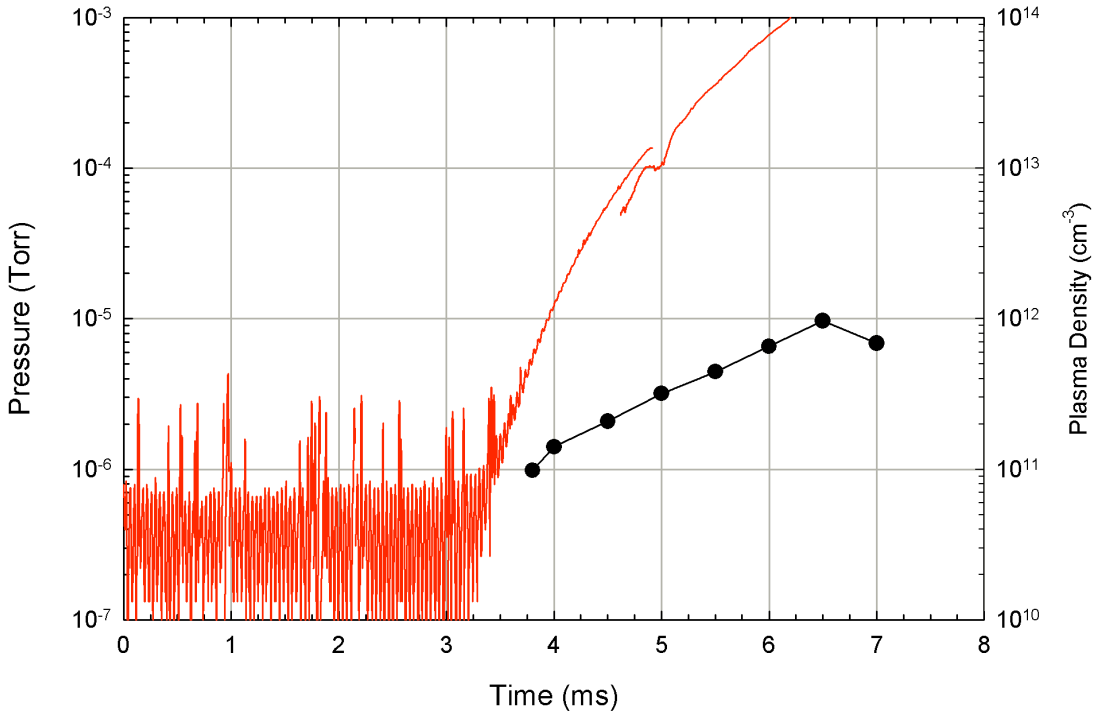

Figure 31. Time evolution of neutral gas pressure and plasma electron density (solid circles) in the pulsed plasma source. One upgrade under consideration is replacing the gas valve with a faster one to reduce the length of the gas puff and the total amount of gas into the system. Another upgrade would be using a pulsed rf supply to increase the rf power level.

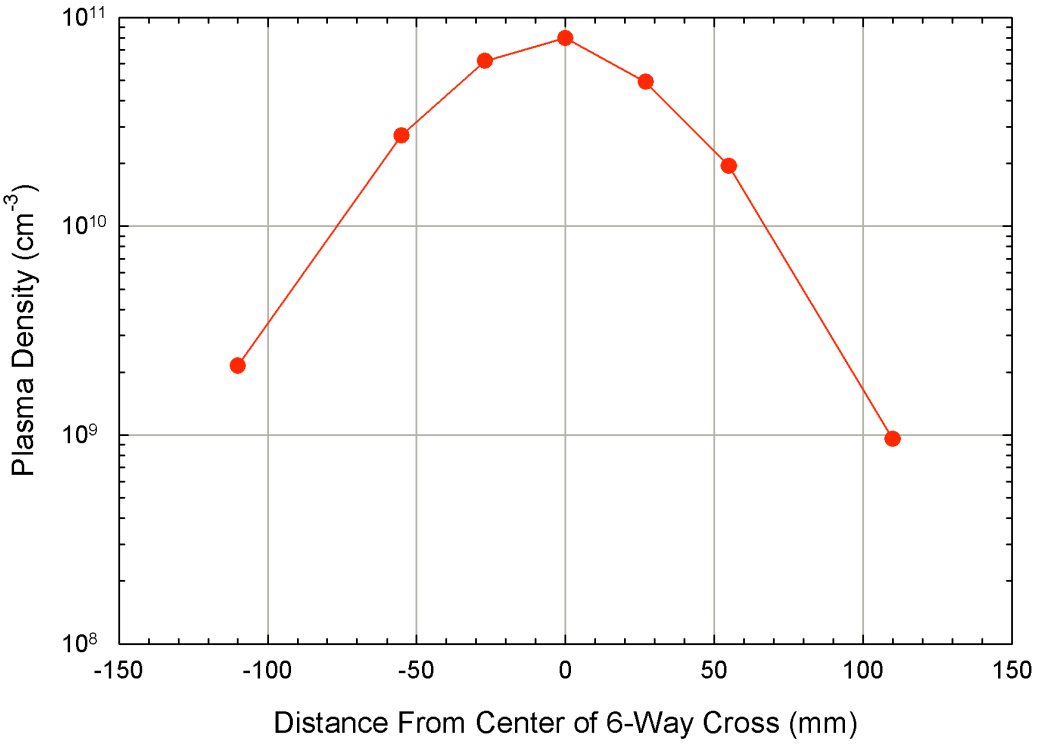

Figure 32. Plasma density profile transverse to the plasma source in the six-way cross.

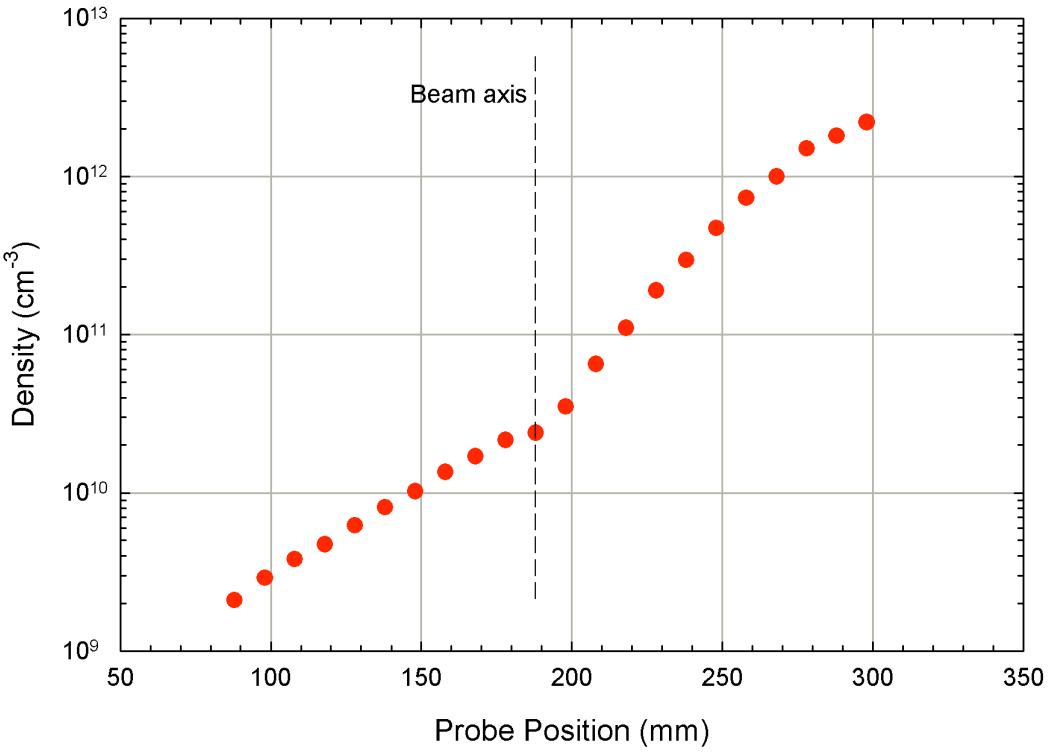

Figure 33. Plasma density in the transverse direction, towards the rf power source, showing a steep gradient.

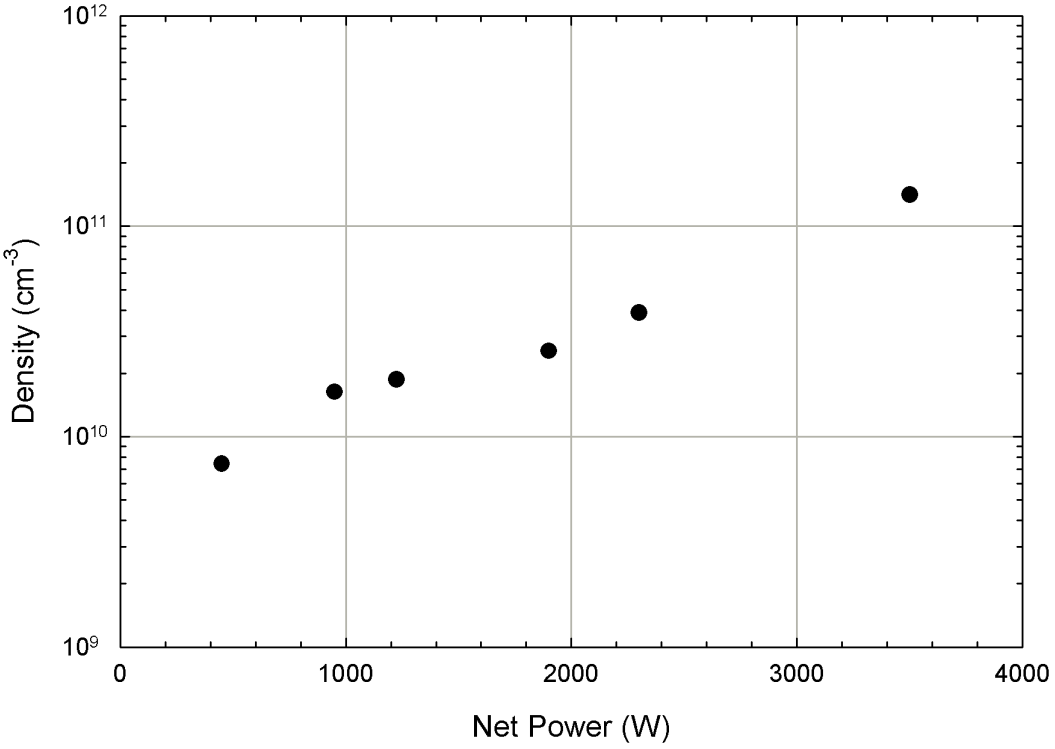

Figure 34. Electron density in the center of the cross as a function of rf power.

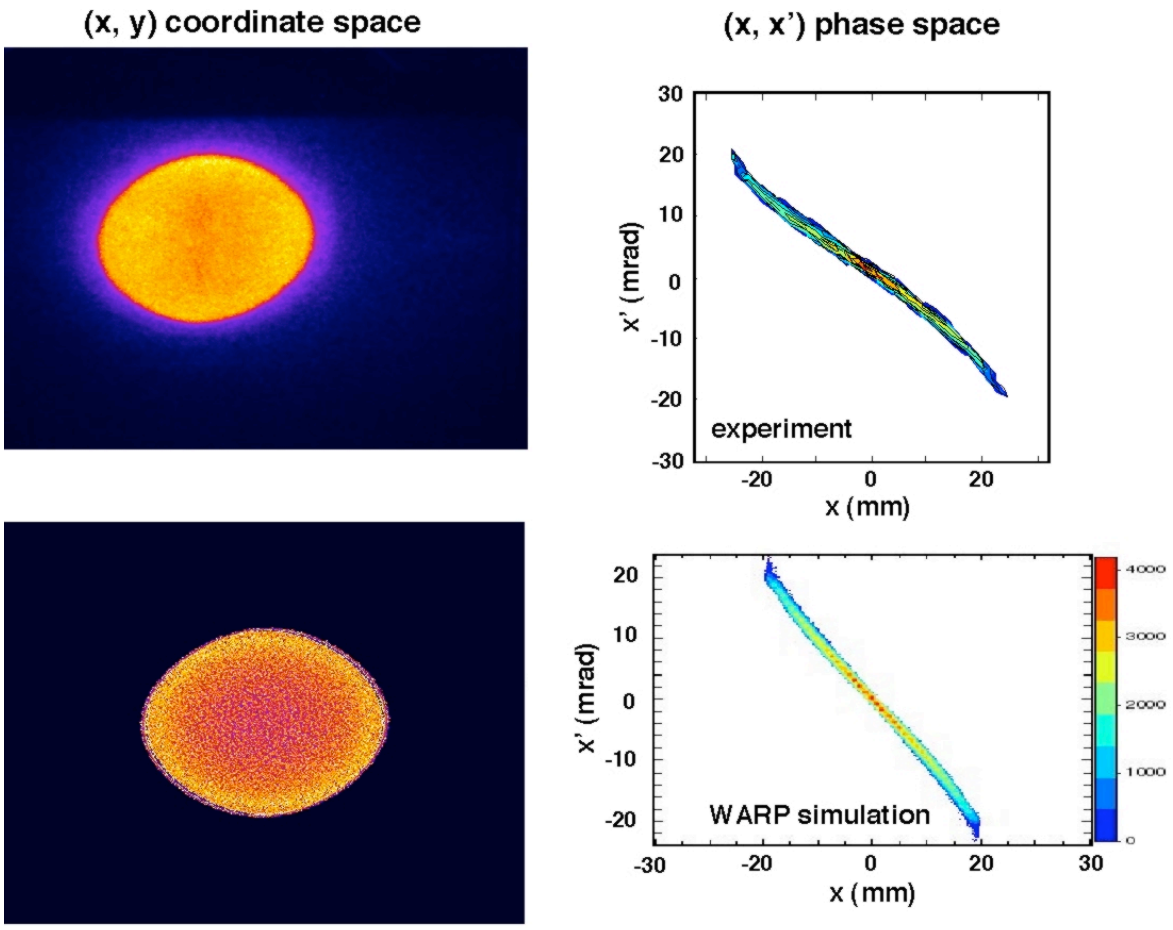

Figure 35. Experimental results and simulations of NTX beam profile and phase-space distribution at exit of channel.

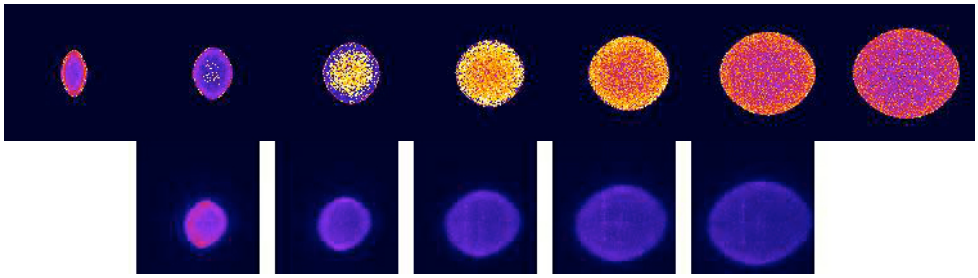

Figure 36, Numerical results (above) and camera images (below) of NTX beam profiles as function of energy.

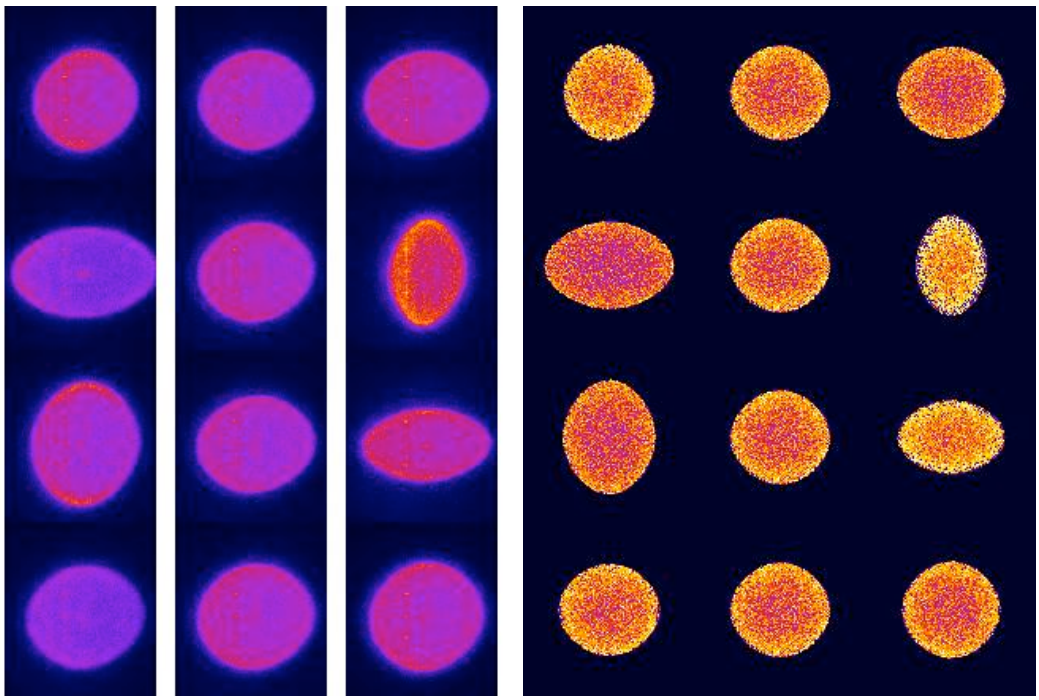

Figure 37. Numerical results (right) and camera images (left) of NTX beam profiles as function of quadrupole field configuration.

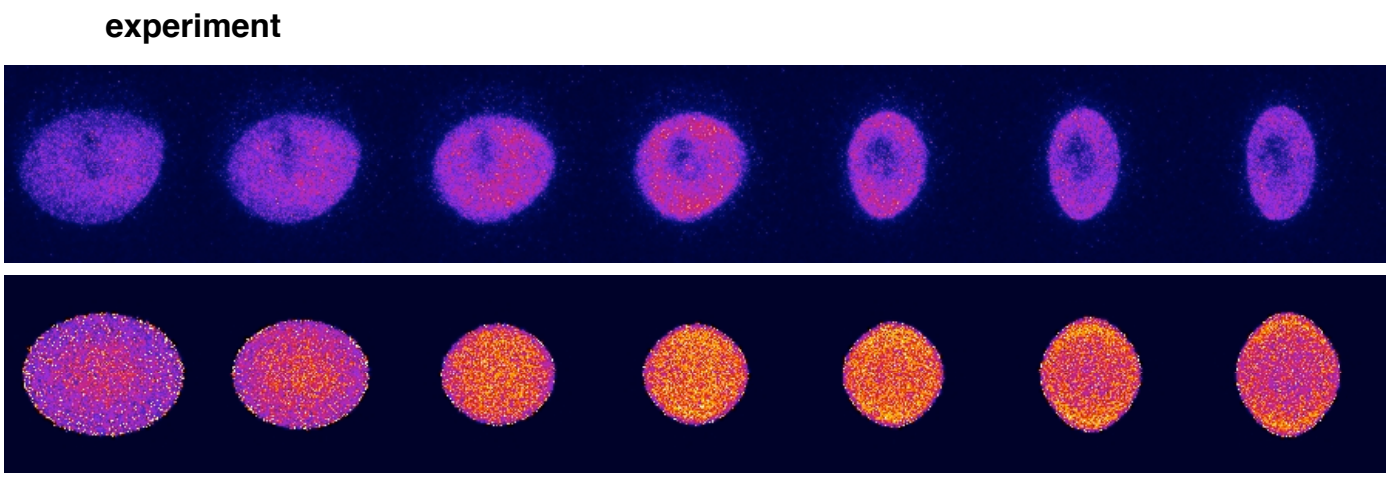

Figure 38. Experimental (top) and theoretical (bottom) NTX beam profiles for a non-neutralized beam 1 m downstream from the exit of the final-focus system.

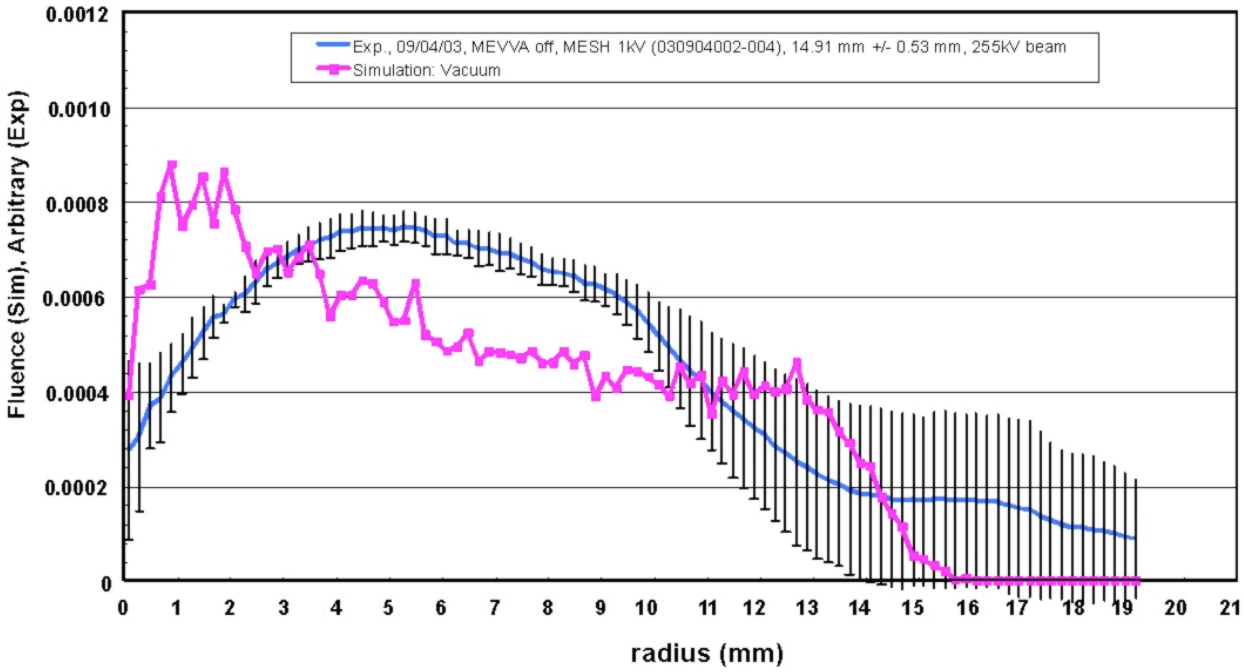

Figure 39. Comparison of a radial density profiles from an unneutralized NTX shot with a theoretical profile from an LSP simulation.

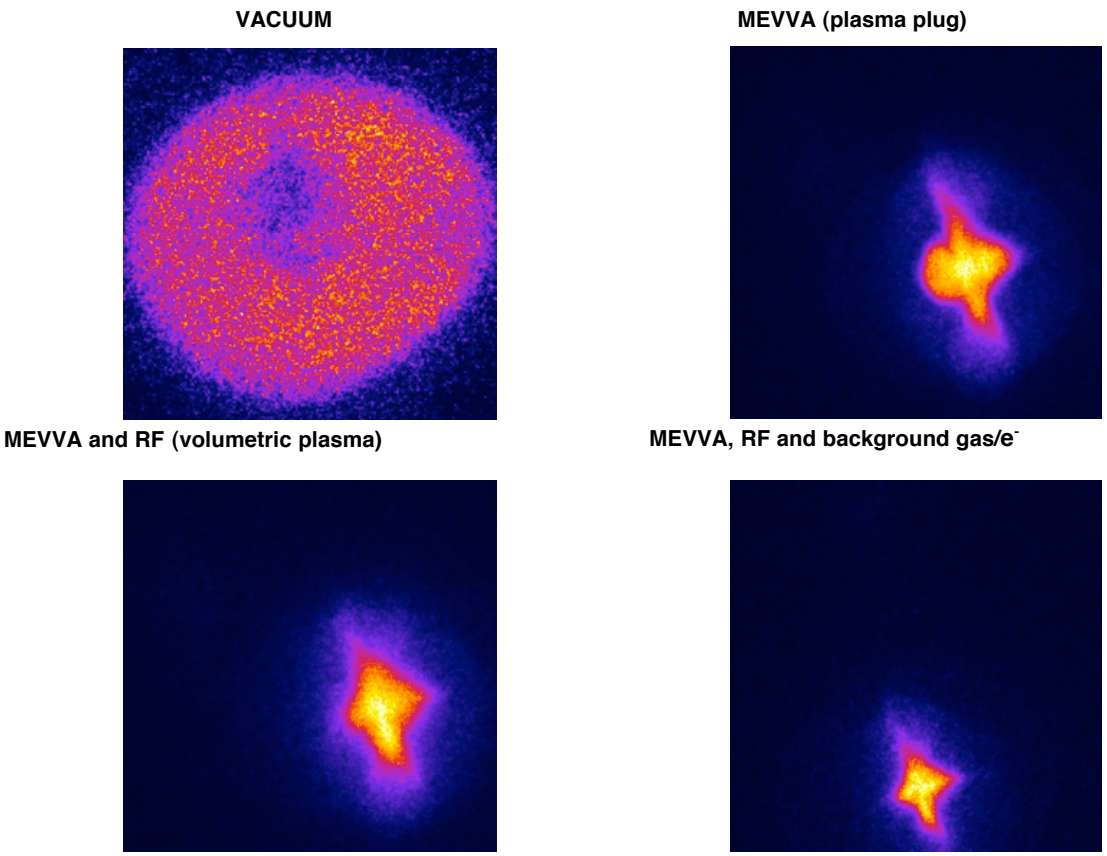

Figure 40. NTX spot-size dependence on neutralization mechanism. All image boxes are 4-cm by 4-cm squares.

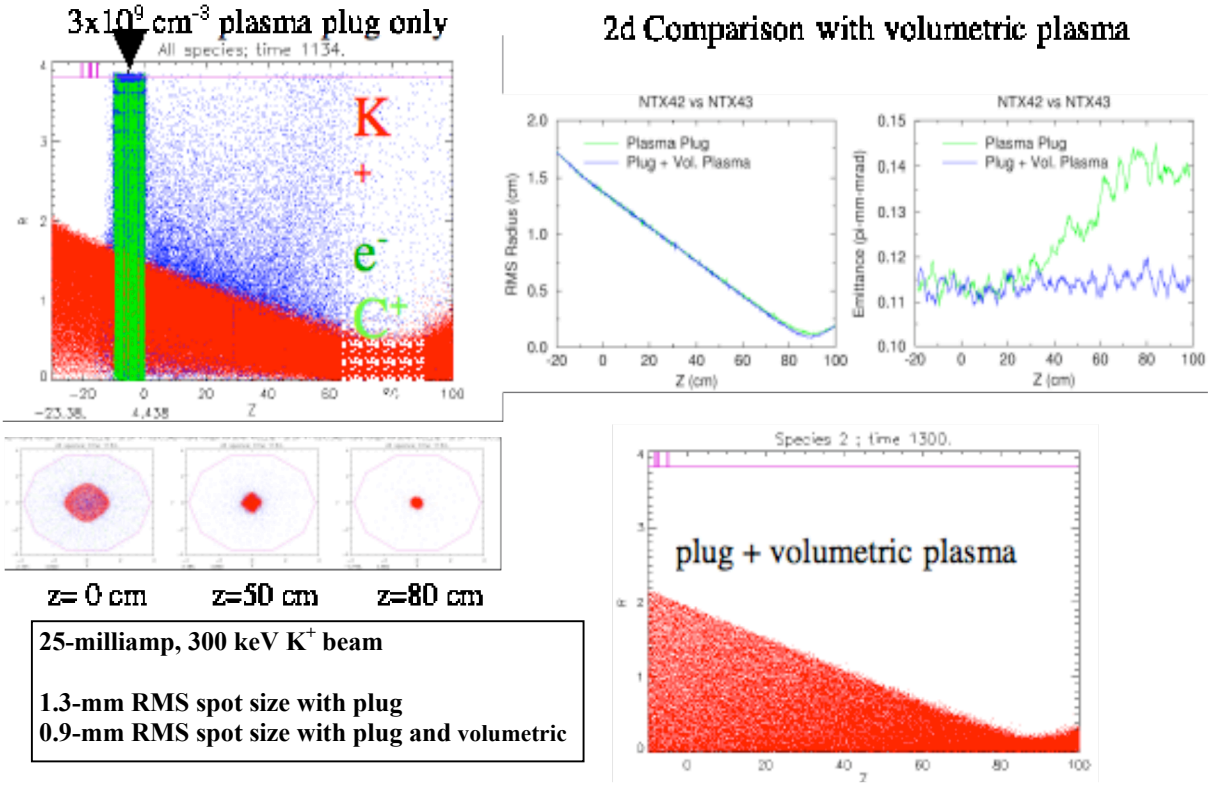

Figure 41. WARP-LSP simulations of NTX with plasma-plug neutralization.

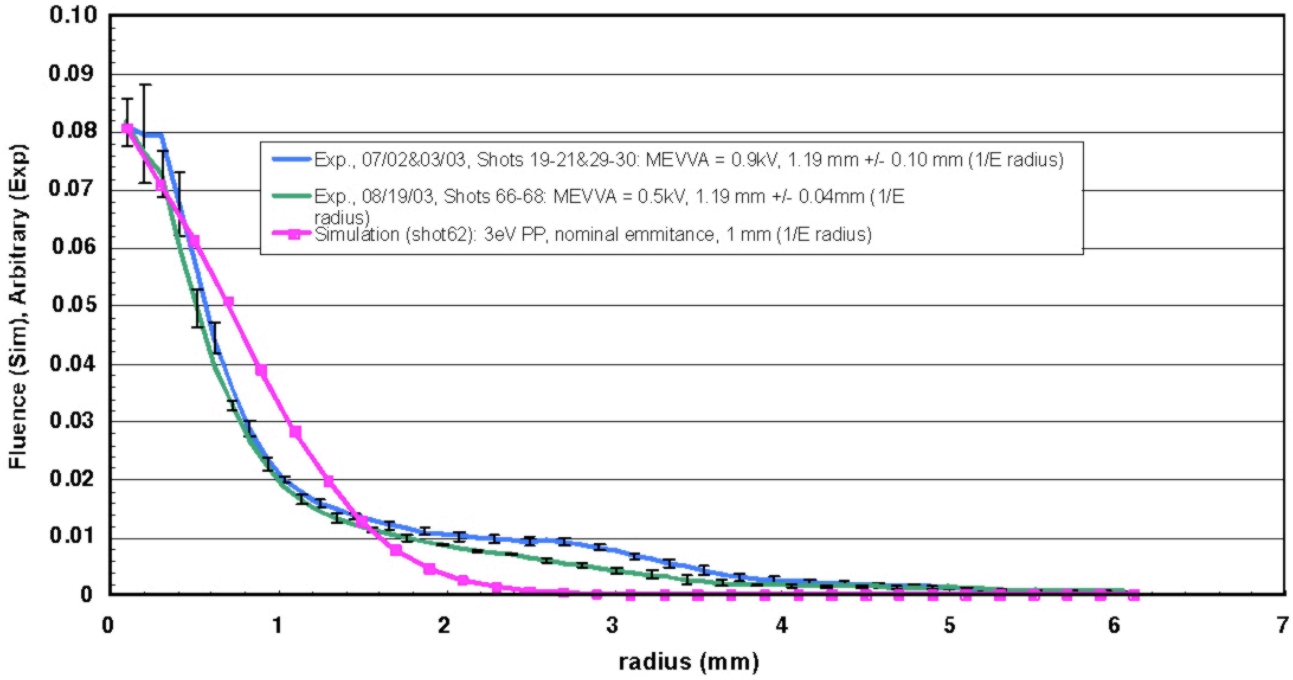

Figure 42. Comparison of radial density profiles from two plasma-neutralized NTX shots with a theoretical profile from an LSP simulation.

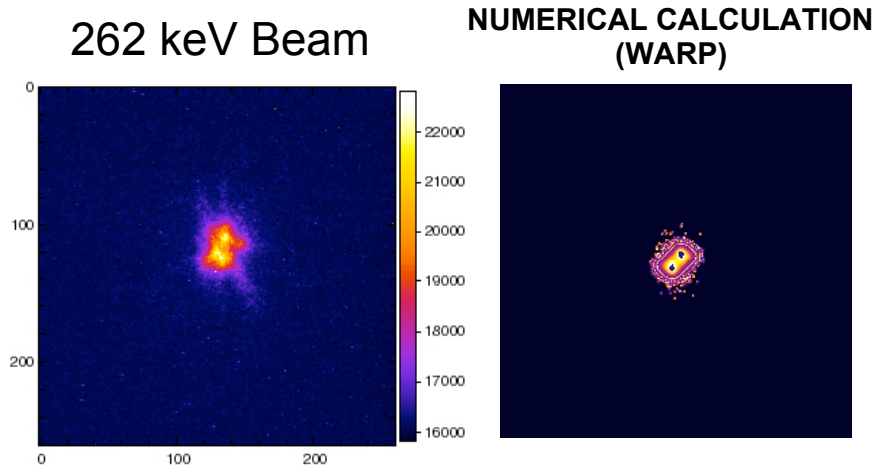

Figure 43. Analog (pinhole) simulation (left) and WARP calculation (right) of fully neutralized NTX beam focused to a small spot. Each image box is a 4-cm by 4-cm square.